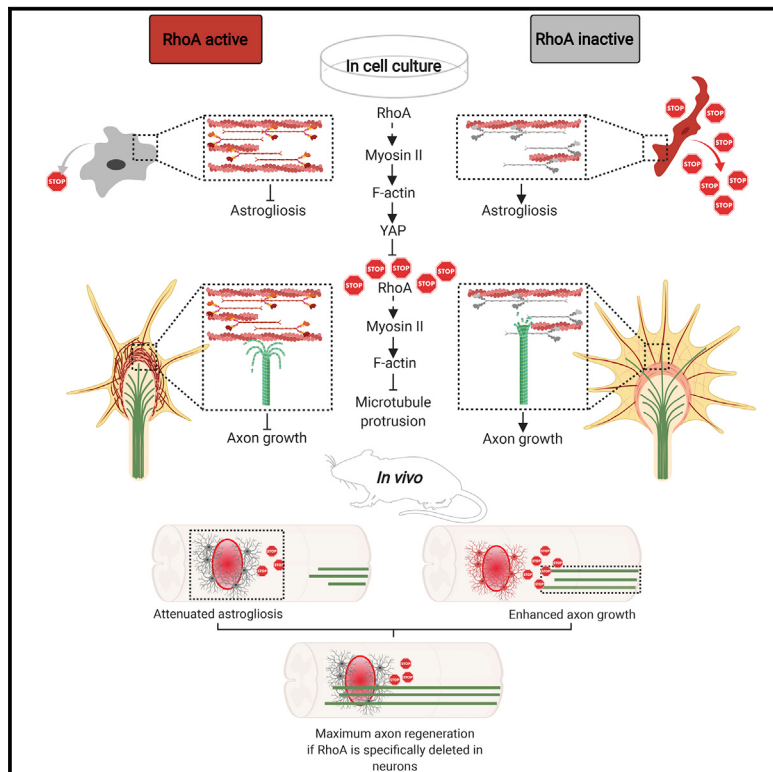


RhoA drives actin compaction to restrict axon regeneration and astrocyte reactivity after CNS injury

Graphical abstract



Authors

Sina Stern, Brett J. Hilton,
Emily R. Burnside, ...,
Jessica M. Gonyer, Cord Brakebusch,
Frank Bradke

Correspondence

frank.bradke@dzne.de

In brief

Stern et al. reveal cell type-specific roles of RhoA that affect axon regeneration in opposite ways. By acting on the cytoskeleton, neuronal RhoA restrains axon regrowth, but astrocytic RhoA attenuates inhibitory astrocyte reactivity. Therefore, only neuron-specific RhoA ablation stimulates regeneration.

Highlights

- RhoA has opposing roles in neurons and astrocytes during CNS regeneration
- Neuronal RhoA prevents axon regeneration by mechanisms that recapitulate polarization
- Astrocytic RhoA drives actin compaction to activate YAP, restricting astrogliosis
- Axon regeneration is only stimulated when RhoA is ablated specifically in neurons



Article

RhoA drives actin compaction to restrict axon regeneration and astrocyte reactivity after CNS injury

Sina Stern,^{1,3} Brett J. Hilton,^{1,3} Emily R. Burnside,¹ Sebastian Dupraz,¹ Emily E. Handley,¹ Jessica M. Gonyer,¹ Cord Brakebusch,² and Frank Bradke^{1,4,*}

¹Laboratory of Axonal Growth and Regeneration, German Center for Neurodegenerative Diseases (DZNE), Venusberg Campus 1/99, 53127 Bonn, Germany

²Biotech Research and Innovation Centre, Biomedical Institute, University of Copenhagen, Ole Maaløes Vej 5, 2200 Copenhagen, Denmark

³These authors contributed equally

⁴Lead contact

*Correspondence: frank.bradke@dzne.de

<https://doi.org/10.1016/j.neuron.2021.08.014>

SUMMARY

An inhibitory extracellular milieu and neuron-intrinsic processes prevent axons from regenerating in the adult central nervous system (CNS). Here we show how the two aspects are interwoven. Genetic loss-of-function experiments determine that the small GTPase RhoA relays extracellular inhibitory signals to the cytoskeleton by adapting mechanisms set in place during neuronal polarization. In response to extracellular inhibitors, neuronal RhoA restricts axon regeneration by activating myosin II to compact actin and, thereby, restrain microtubule protrusion. However, astrocytic RhoA restricts injury-induced astrogliosis through myosin II independent of microtubules by activating Yes-activated protein (YAP) signaling. Cell-type-specific deletion in spinal-cord-injured mice shows that neuronal RhoA activation prevents axon regeneration, whereas astrocytic RhoA is beneficial for regenerating axons. These data demonstrate how extracellular inhibitors regulate axon regeneration, shed light on the capacity of reactive astrocytes to be growth inhibitory after CNS injury, and reveal cell-specific RhoA targeting as a promising therapeutic avenue.

INTRODUCTION

After injury to the central nervous system (CNS), axons fail to regenerate. Extrinsic growth-inhibitory factors surrounding the injured axon and intrinsic neuronal processes prevent regeneration (Curcio and Bradke, 2018; He and Jin, 2016; Quraishe et al., 2018; Schwab and Strittmatter, 2014; Silver and Silver, 2014). Although extrinsic growth-inhibitory factors are thought to instruct the diminished neuron-intrinsic growth capacity after injury, how these extrinsic and intrinsic pathways are connected is largely unclear. We investigated the physiological intracellular mechanisms that could link to extracellular inhibitory signaling to mediate growth restraint.

The small GTPase ras homolog gene family member A (RhoA) is a node onto which extracellular inhibitory signals, including chondroitin sulfate proteoglycans (CSPGs) and CNS myelin, converge (Boueid et al., 2020; Hu and Selzer, 2017; Sami et al., 2020). However, the effector mechanisms that ultimately mediate axon growth restraint have remained undefined (Geoffroy and Zheng, 2014; Sami et al., 2020). One reason for this is that manipulation of RhoA by non-endogenous compounds or by overexpression of its mutant forms leads to stimulation of

additional signaling pathways; for example, by scavenging guanine nucleotide exchange factors (GEFs) and GTPase-activating proteins (GAPs) of other Rho GTPases (Pertz, 2010), activating a myriad of additional RhoA-independent effectors. Thus, even though inactivation of RhoA by the bacterial toxin C3 exoenzyme after spinal cord injury enables axon regeneration (Dergham et al., 2002; Duffy et al., 2009; Lehmann et al., 1999), which rationalized phase II clinical trials (Fehlings et al., 2018), the physiological role of RhoA after CNS injury has remained unclear (Fujita and Yamashita, 2014; Geoffroy and Zheng, 2014; Griffin and Bradke, 2020). Consequently, the trials were discontinued (Fehlings et al., 2021). We therefore used RhoA knockout mouse models to investigate the physiological mechanisms and identify the physiological effectors underlying growth restraint in the injured adult CNS.

Cytoskeletal dynamics critically regulate axon growth during development and axon regeneration in the injured adult CNS (Blanque and Bradke, 2018). Although some signaling pathways appear to solely function in developmental growth or axon regeneration (Jones et al., 2006; Liu and Snider, 2001; Renthal et al., 2020; Uvdadia et al., 2001), we hypothesized that mechanisms that prevent axons from regenerating in the adult nervous



system might recapitulate processes that restrict axon growth during neuronal development (Hilton and Bradke, 2017). During neuronal polarization in embryonic development, RhoA decelerates axon growth by initiating actin arc formation through the actin motor myosin II, which restrains microtubule protrusion (Dupraz et al., 2019). Because microtubules are decisive for axon regeneration (Ertürk et al., 2007), and their pharmacological stabilization induces axon regeneration in the injured spinal cord (He et al., 2016; Hellal et al., 2011; Kondo et al., 2019; Nagai et al., 2016; Ruschel and Bradke, 2018; Ruschel et al., 2015), we hypothesized that RhoA signaling may ultimately regulate microtubule dynamics to control the regenerative state.

Glia cells also play a crucial and complex role in CNS regeneration. In particular, astrocytes have been attributed different, often opposing functions in axon growth (Burda and Sofroniew, 2014; Cregg et al., 2014; Liddelow and Barres, 2017). Astrocytes are thought to inhibit axon growth by secreting CSPGs (Hara et al., 2017; McKeon et al., 1991; Schachtrup et al., 2010). Indeed, reactive astrocytes could potentially be the reason why injured axons acquiring growth competence fail to cross a mechanical lesion-induced glial scar but not a minimal 2-photon laser lesion lacking a glial scar (Ylera et al., 2009). However, more recent studies have supported the idea that reactive astrocytes are permissive for regenerating axons (Anderson et al., 2016, 2018). To define the role of reactive astrocytes in axon regeneration, molecular regulators driving astrocyte reactivity in such a proposed inhibitory state need to be identified. As pharmacological inhibition of RhoA and its downstream targets enhances astrocyte reactivity and CSPG expression (Chan et al., 2007; Racchetti et al., 2012), astrocytic RhoA might control the regenerative state of injured axons.

Here we uncover, by cell-type-specific genetic ablation, that RhoA has roles in neurons and astrocytes that affect axon regeneration oppositely. In neurons, inhibitory factors activate myosin II in a RhoA-dependent fashion, compacting actin to block microtubule protrusion and inhibiting axon regrowth. In astrocytes, however, RhoA limits astrogliosis and anti-regenerative action by suppressing Yes-activated protein (YAP) signaling through actin-mediated compaction but independent of microtubules. Thus, simultaneous deletion of RhoA in neurons and astrocytes does not promote axon regeneration after CNS injury, but neuron-specific RhoA deletion does. Our data reveal missing mechanisms of a key signaling cascade restraining axon growth and highlight the importance of developing cell-type-specific strategies to promote regeneration.

RESULTS

RhoA restrains neurite growth on inhibitory substrates

Inhibitory cues that prevent axon regeneration in adulthood, including CNS myelin and CSPGs, inhibit growth of late postnatal but not early postnatal or embryonic neurons (DeBellard et al., 1996). Therefore, to determine the physiological role of RhoA in growth inhibition after CNS injury, we used late postnatal cerebellar granule neurons (CGNs), a standard paradigm to test for growth inhibition (Ertürk et al., 2007; Hellal et al., 2011; Mukhopadhyay et al., 1994), of *nestin-cre*^{tg/-}, *rhoA*^{f/f} mice (Dupraz et al., 2019), hereafter called RhoANes knockout (RhoANesKO) mice (Figure 1A). Immunoblot analysis confirmed the absence of

RhoA protein in cerebellar tissue extracts of RhoANesKO mice (Figure 1B). Consistent with the role of RhoA in constraining axon growth during embryonic development, RhoA ablation enhanced the growth of post-natal day 1 (P1)–P2 CGNs on permissive substrates relative to control *nestin-cre*^{-/-}, *rhoA*^{f/f} (hereafter called wild-type [WT]) neurons (Figures S1A and S1B). Conversely, P6–P10 CGNs derived from RhoANesKO mice and from WT mice showed similar neurite lengths when plated on growth-permissive substrates (Figures 1C–1E). However, RhoANesKO and WT neurons differed in their growth on inhibitory substrates. When plated on CSPGs or CNS myelin extract, RhoANesKO neurons grew longer neurites than WT neurons (Figures 1C–1E). Re-expression of WT RhoA fused to EGFP (RhoAWT) in RhoANesKO neurons restored growth restraint on CSPGs to the extent found in WT neurons (Figures S1C and S1D). Similarly, adult dorsal root ganglion (DRG) RhoANesKO neurons grew longer axons on CSPGs or CNS myelin extract than WT DRG neurons (Figures S1E–S1G). Thus, RhoA is a physiological mediator of growth restraint in response to extracellular inhibitors.

Inhibitory cues decrease growth cone size and dynamics through RhoA

Because the growth cone drives neurite outgrowth (Coles and Bradke, 2015; Dent et al., 2011), we hypothesized that RhoA inhibits growth by restraining growth cone dynamics. Time-lapse microscopy showed that, when plated on CSPGs, growth cones of WT neurons were reduced in size and contained fewer lamellipodia than those grown on growth-permissive laminin (Figures 1F and 1G; Video S1). WT growth cones were also less dynamic on CSPGs than on laminin (Figures 1F and 1H; Video S1). In contrast, RhoANesKO neurons preserved a large growth cone area with dynamic lamellipodia when grown on CSPGs (Figures 1F–1H; Video S1). Thus, inhibitory cues signal through RhoA to restrict growth cone dynamics.

RhoA inhibits neurite growth by enhancing F-actin density

Growth cone dynamics are dictated by the actin cytoskeleton (Gomez and Letourneau, 2014; Omotade et al., 2017; Schelski and Bradke, 2017). Hence, we hypothesized that exposure to inhibitory substrates leads to RhoA-mediated changes in growth cone actin cytoskeletal structure (Figure 2A). Phalloidin staining of fixed cells showed an increase in filamentous (F)-actin density in WT growth cones exposed to CSPGs and myelin compared with growth cones of neurons plated on a permissive control substrate (Figures 2B–2D). This increase was RhoA-dependent because RhoANesKO neurons lacked such an increase in growth cone F-actin upon CSPG or myelin exposure (Figures 2B–2D). High-resolution imaging revealed that growth of neurons on inhibitory CSPGs induced actin condensation in their growth cones and that RhoANesKO reduced this effect (Figures S1H and S1I). In line with this, live-cell microscopy of LifeAct-transfected neurons to visualize actin dynamics confirmed that, upon exposure to CSPGs, actin became rapidly condensed in WT but not in RhoANesKO growth cones (Video S2). Moreover, biochemical extracts of cultured neurons validated that the F-actin to globular (G)-actin ratio increased upon CSPG exposure in WT but not in RhoANesKO cells (Figures 2E and 2F).

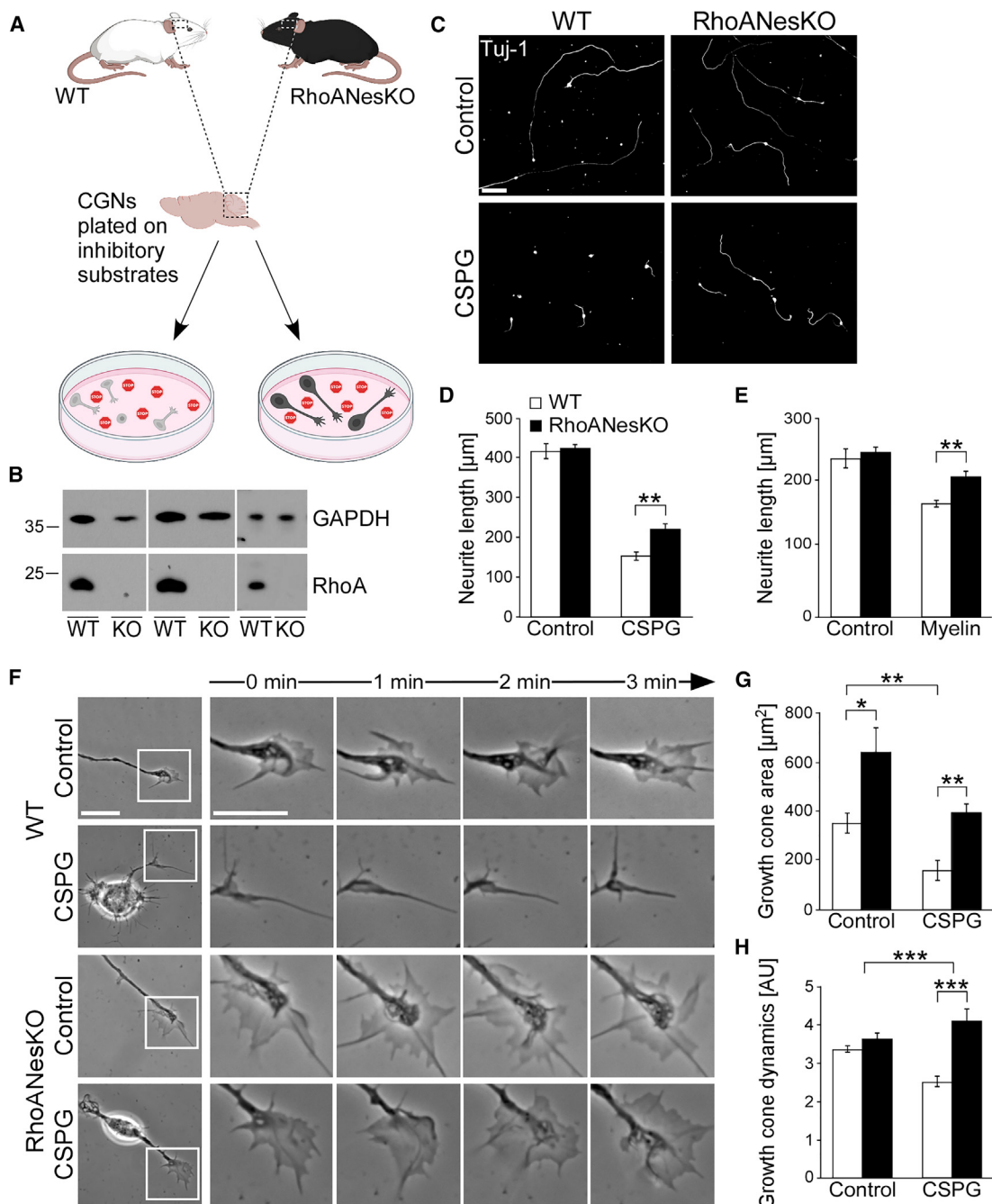


Figure 1. RhoA deletion promotes neurite growth on inhibitory substrates

(A) Scheme of RhoANesKO mouse breeding and the neurite outgrowth assay using primary cerebellar granule neurons (CGNs).

(B) Immunoblot of RhoA in WT and RhoANesKO cerebellar tissue extracts. Glyceraldehyde-3-phosphate dehydrogenase (GAPDH) is shown as a loading control.

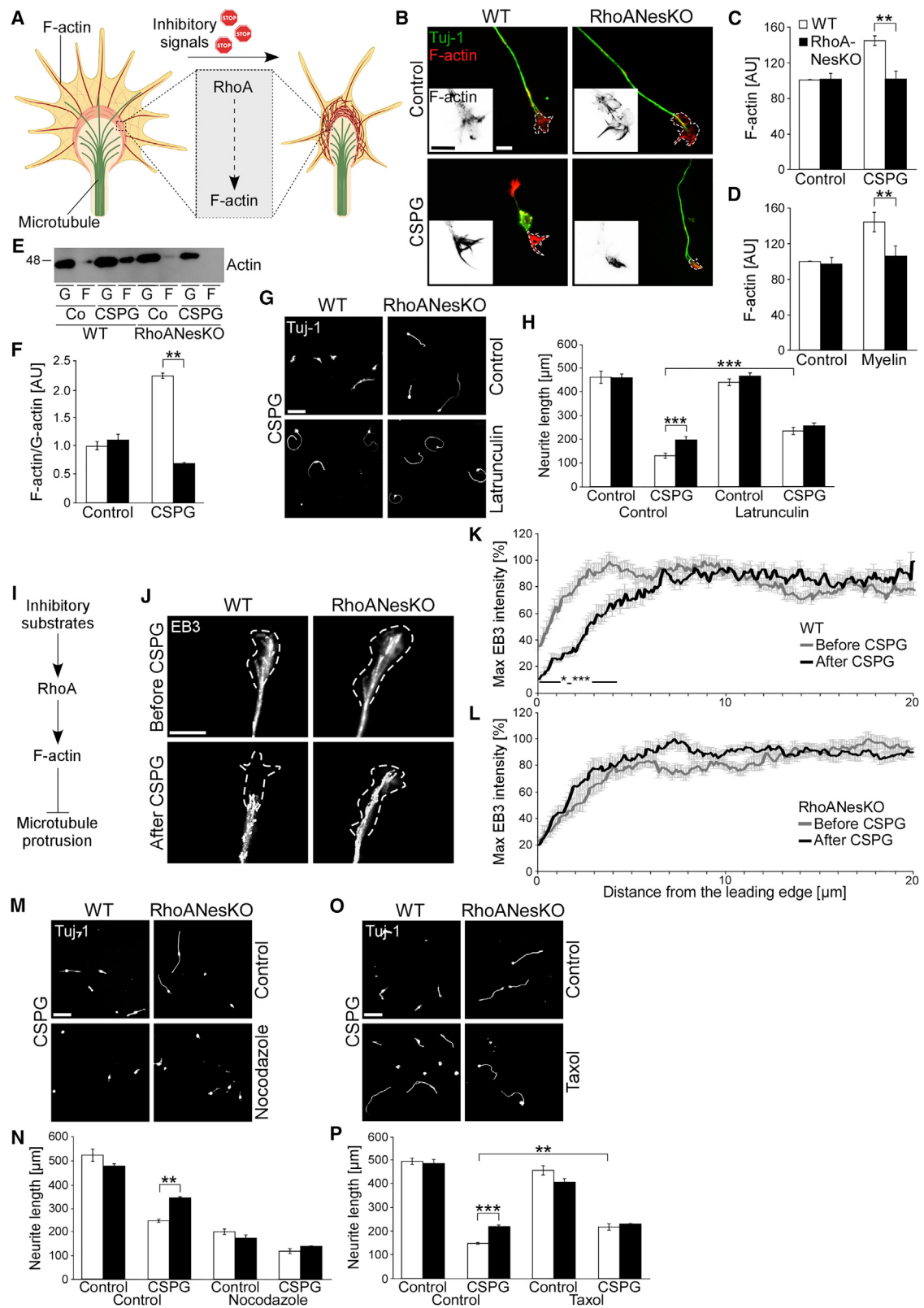
(C) Representative fluorescence images of Tuj-1 antibody-stained CGNs derived from WT or RhoANesKO mice (post-natal day 6 (P6)–P10) grown in the absence (control) or presence of CSPGs. Scale bar, 40 μm .

(D and E) Mean neurite length of CGNs grown on control or CSPGs (D) or on control or total myelin (E). All values are plotted as mean \pm SEM. **p < 0.01 by Student's t test. n = 5 independent experiments, N = 473 (D) or 591 (E) cells.

(F) Live-cell imaging of CGNs derived from WT or RhoANesKO mice and grown on control substrate or CSPGs. Insets show growth cones at the start of recording (0 min) as well as 1, 2, and 3 min later. Scale bar, 5 μm .

(G and H) Quantification of (F). Shown are growth cone areas (G) and dynamics (H) of WT and RhoANesKO neurons grown on control substrate or CSPGs. Values are plotted as mean and SEM. *p < 0.05, **p < 0.01, ***p < 0.001 by Student's t test. n = 6 individual cell cultures, N = 116 cells.

See also Figure S1 and Video S1.



(legend on next page)

A dense filamentous actin network decreases neurite growth by preventing microtubules from protruding to the growth cone leading edge (Bradke and Dotti, 1999; Flynn et al., 2012; Kunda et al., 2001; Figure 2A). We therefore hypothesized that inhibitory substrates restrict growth by enhancing F-actin density. To test this, we treated neurons plated on inhibitory CSPGs with the actin-depolymerizing drug latrunculin B. Drug-treated WT neurons, which showed the typical curved morphology upon actin depolymerization (Bentley and Toroian-Raymond, 1986; Bradke and Dotti, 1999; Chia et al., 2016), grew longer neurites on CSPGs than those that were vehicle treated, and they reached lengths equivalent to neurites of RhoANesKO neurons (Figures 2G and 2H). RhoANesKO neurons, however, had no additional increase in length with latrunculin B treatment (Figures 2G and 2H). These data suggest that growth inhibitory factors induce RhoA-mediated actin compaction to restrain neurite growth.

RhoA-dependent microtubule destabilization impairs microtubule protrusion and, consequently, neurite growth on inhibitory substrates

In postnatal neurons exposed to inhibitory cues, RhoA-dependent differences occurred. We hypothesized that, in these cells, RhoA-driven actomyosin changes restrict microtubule protrusion to the growth cone leading edge to restrain axon regrowth (Figures 2A and 2I). To test this, we performed live-cell imaging of the growth cones of WT and RhoANesKO neurons transfected with microtubule end binding protein 3 (EB3) fused to the fluorophore mCherry (Flynn et al., 2012) during CSPG delivery. Polymerizing microtubule ends of WT and RhoANesKO neurons infiltrated the growth cone leading edge prior to CSPG exposure

(Figures 2J–2L; Video S2). However, in WT neurons, addition of CSPGs caused microtubules to retract from the growth cone leading edge (Figures 2J and 2K; Video S2). In contrast, even after CSPG exposure, the microtubules of RhoANesKO neurons continued to infiltrate the growth cone leading edge (Figures 2J and 2L; Video S2).

To directly test the involvement of microtubules in RhoA-mediated growth arrest elicited by inhibitory factors, we assessed whether microtubule destabilization with the microtubule-depolymerizing drug nocodazole in RhoANesKO neurons restored the reduced neurite growth observed in WT neurons on CSPGs. Indeed, in RhoANesKO neurons, nocodazole treatment abolished the knockout-dependent increase in neurite growth on inhibitory CSPGs (Figures 2M and 2N). Conversely, moderate stabilization of microtubules with the drug Taxol enhanced outgrowth of WT neurons so that their neurites were equivalent in length to the neurites of vehicle-treated RhoANesKO neurons on CSPGs (Figures 2O and 2P). Moreover, in RhoANesKO neurons, Taxol treatment had no additive effect on neurite length (Figures 2O and 2P). Thus, in response to inhibitory substrates, RhoA increases F-actin density in the growth cone, which prevents microtubules from protruding to the leading edge, restraining neurite growth.

RhoA-mediated growth inhibition depends on myosin II activation

RhoA could enhance F-actin density to restrain microtubule protrusion through a variety of downstream effectors. For example, RhoA affects the actin cytoskeleton by activating Rho-kinase (ROCK), which, in turn, via phosphorylation, leads to inactivation

Figure 2. RhoA increases F-actin density to impair microtubule protrusion and, consequently, neurite outgrowth on inhibitory substrates

- (A) Scheme of growth cone morphology and signaling changes after stimulation with inhibitory molecules.
- (B) Representative fluorescence images of CGNs derived from WT and RhoANesKO mice grown in the absence (control) or presence of CSPGs stained with Tuj-1 and phalloidin antibodies to visualize microtubules and F-actin, respectively. Insets show F-actin staining of growth cones. The region of interest used for F-actin quantification is outlined. Scale bar, 5 μ m.
- (C) Quantification of (B). Shown is F-actin intensity of growth cones grown on control substrate compared with CSPGs. Values are plotted as mean \pm SEM and normalized to the corresponding WT control. **p < 0.01 by Student's t test. n = 5 individual cultures, N = 938 cells.
- (D) Quantification of F-actin intensity of growth cones grown on control substrate compared with purified total myelin (representative images not shown). Values are plotted as mean \pm SEM and normalized to the corresponding WT control. **p < 0.01 by Student's t test. n = 5 individual cultures, N = 868 cells.
- (E) Immunoblot for F- and G-actin expression in RhoANesKO and WT CGNs grown in the absence (control) or presence of CSPGs.
- (F) Quantification of F- to G-actin ratio shown in (E). The band at 48 kDa was used for quantification. Values are plotted as mean \pm SEM. **p < 0.01 by Student's t test. n = 3 individual cultures.
- (G) Representative fluorescence images of WT and RhoANesKO CGNs stained with Tuj-1 antibody following administration of DMSO (control) or latrunculin B. Scale bar, 40 μ m.
- (H) Quantification of (G). Values are plotted as mean \pm SEM. ***p < 0.01 by Student's t test. n = 6 individual cultures, N = 1,510 cells.
- (I) Scheme of signaling changes after stimulation with inhibitory molecules.
- (J) Representative images during live cell imaging of the microtubule end tip marker EB3-mCherry in WT and RhoANesKO CGNs before and after administration of CSPGs. Scale bar, 5 μ m.
- (K and L) Maximum EB3 intensity in WT (K) and RhoANesKO (L) neurons before and after administration of CSPGs. Error bars represent SEM. *p < 0.05, **p < 0.01, ***p < 0.001 by Student's t test. n = 7 individual cultures, N = 35 cells.
- (M) Representative fluorescence images of WT and RhoANesKO CGNs grown on CSPGs and stained with Tuj-1 antibody after administration of DMSO (control) or the microtubule-destabilizing drug nocodazole. Scale bar, 40 μ m.
- (N) Quantification of (M). Shown is neurite outgrowth of WT and RhoANesKO neurons treated with nocodazole and grown in the absence (control) or presence of CSPGs. The average length of the longest neurite was measured. Values are plotted as mean \pm SEM. **p < 0.01 by Student's t test. n = 3 individual cultures, N = 865 cells.
- (O) Representative fluorescence images of WT and RhoANesKO CGNs grown on CSPGs and stained with Tuj-1 antibody after administration of DMSO (control) or taxol. Scale bar, 40 μ m.
- (P) Quantification of (O). Shown is neurite outgrowth of WT and RhoANesKO neurons treated with taxol and grown in the absence (control) or presence of CSPGs. Values are plotted as mean \pm SEM. **p < 0.01, ***p < 0.001 by Student's t test. n = 4 individual cultures, N = 1,045 cells.

See also Figure S1 and Video S2.

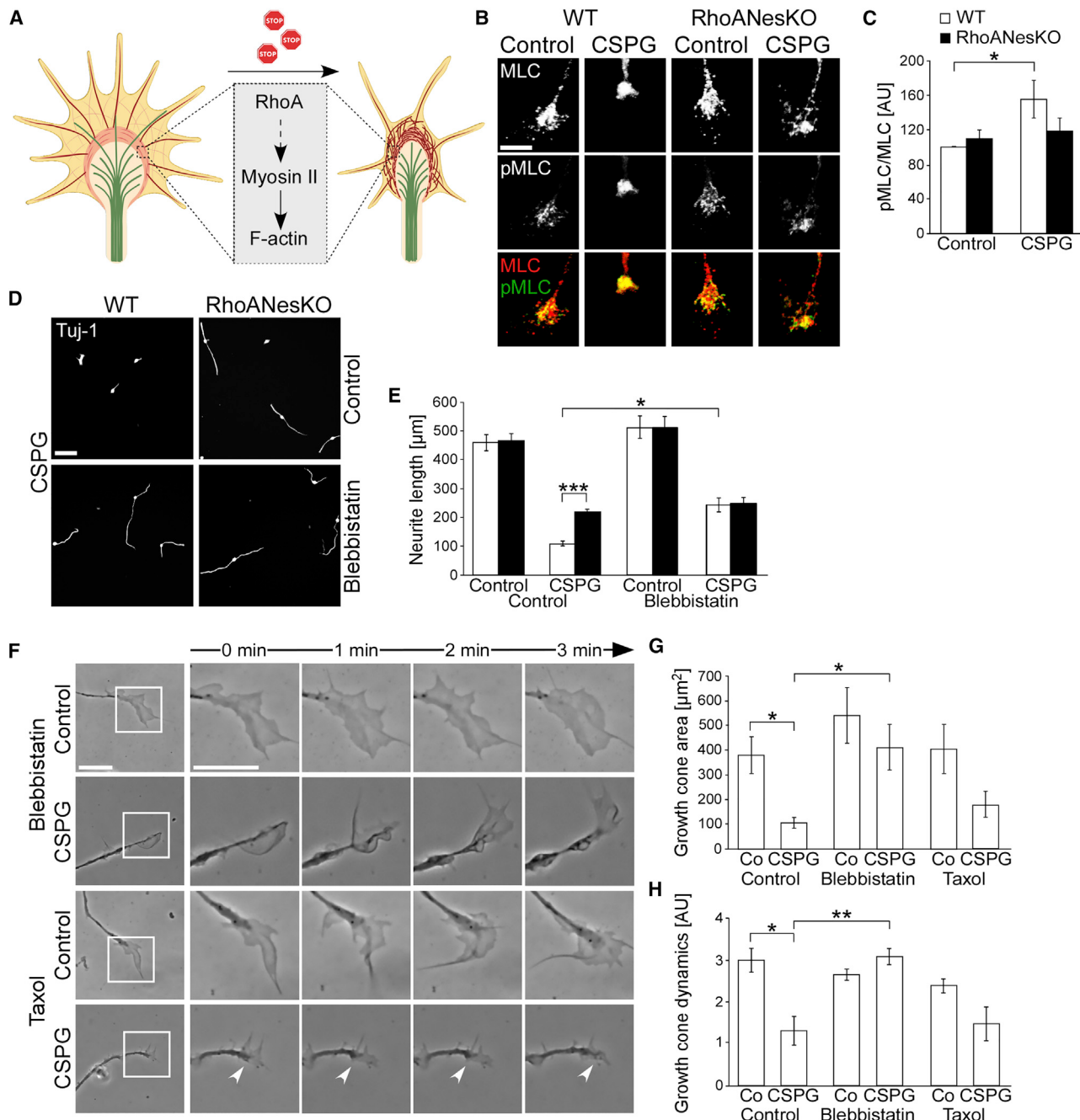


Figure 3. RhoA-mediated growth inhibition depends on myosin II

(A) Scheme of growth cone signaling pathways after stimulation with inhibitory molecules.

(B) Representative fluorescence images of WT and RhoANesKO neurons grown in the absence (control) or presence of CSPGs and stained with total myosin light chain (MLC) subunit and phosphorylated MLC (pMLC) subunit antibodies. Scale bar, 5 μm.

(C) Quantification of (B). Shown is the average mean intensity of the pMLC/MLC ratio in WT and RhoANesKO growth cones on control substrate and CSPGs. Values are plotted as mean \pm SEM and normalized to the WT control. * $p < 0.05$ by Student's t test. n = 4 individual cultures, N = 400 cells.

(D) Representative fluorescence images of WT and RhoANesKO neurons grown in the presence of CSPGs and treated with DMSO (control) or blebbistatin 4 h after plating and stained with Tuj-1 antibody. Scale bar, 40 μm.

(E) Quantification of (D). Shown are WT and RhoANesKO neurons grown in the absence (control) or presence of CSPGs and treated with DMSO (control) or blebbistatin. Values are plotted as mean \pm SEM. * $p < 0.05$, *** $p < 0.001$ by Student's t test. n = 4 individual cultures, N = 1,328 cells.

(legend continued on next page)

of cofilin and activation of the actin motor myosin II (Luo, 2000). Cofilin depolymerizes and severs F-actin filaments so that its inactivity causes an increase in F-actin (Flynn et al., 2012; Sarmiere and Bamburg, 2004) and its activation promotes regeneration (Tedeschi et al., 2019). Therefore, we assessed whether growth inhibitors signal through RhoA to enhance F-actin density in the growth cone by inactivating cofilin. Immunocytochemistry analysis showed that exposure to CSPGs indeed enhanced cofilin phosphorylation and inactivation in the growth cones of WT neurons (Figures S2A and S2B). However, this CSPG-induced phosphorylation was independent of RhoA because it also occurred in the growth cones of RhoANesKO neurons (Figures S2A and S2B). Thus, inhibitory cues inactivate cofilin but do so independent of RhoA signaling. Consistent with this finding, overexpression of cofilin in RhoANesKO neurons stimulated additional neurite outgrowth (Figures S2C and S2D).

RhoA can also enhance F-actin density through myosin II, which is activated by phosphorylation of the myosin light chain (MLC) (Figure 3A). Inactivation of myosin II leads to axon regeneration (Wang et al., 2020), and RhoA activation of myosin II controls developmental axon growth (Dupraz et al., 2019). We therefore wanted to find out whether postnatal neurons exploit a signaling mechanism that is active during development to respond to inhibitory cues. Immunocytochemistry revealed an increase in phosphorylated MLC in WT but not RhoANesKO neurons exposed to CSPGs (Figures 3B and 3C), suggesting that inhibitory substrates activate myosin II through RhoA. Overexpression of a constitutively active mutant of the regulatory subunit of myosin II fused to EGFP (MLCcα) reduced neurite growth in RhoANesKO neurons and restored their phenotype to that found in WT neurons exposed to CSPGs (Figures S2E and S2F).

We hypothesized that if RhoA-dependent growth inhibition triggered by inhibitory factors is mediated through myosin II, inactivation of myosin II would enhance the growth of WT but not of RhoANesKO neurons exposed to inhibitory signals. Consistent with previous results (Hur et al., 2011; Yu et al., 2012), treatment with the myosin II inhibitor blebbistatin, which blocks myosin heavy chain in its actin-detached conformation, enhanced neurite growth of WT neurons in the presence of CSPGs (Figures 3D and 3E). In line with the hypothesis that myosin II acts downstream of RhoA to mediate growth inhibition, blebbistatin treatment had no additive effect on neurite length in RhoANesKO neurons (Figures 3D and 3E). Moreover, live-cell microscopy showed that blebbistatin-treated WT growth cones resembled the dynamics of RhoANesKO growth cones and formed lamellipodia in the presence of inhibitory CSPGs (Figures 3F–3H; Video S3). Consistent with our finding that microtubules act downstream of myosin II, Taxol did not restore lamellipodium formation but induced the central microtubule-rich domain of the growth cone to extend closer to the leading edge in WT neurons (Figures 3F–3H; Video S3). Our data show how inhibitory signals converge on the RhoA-mediated signaling cascade that inhibits

neurite growth. RhoA activates myosin II to induce actin compaction, which restrains microtubules from protruding to the neurite leading edge.

Axons of mice deficient in RhoA in neurons and astrocytes fail to regenerate after CNS injury

Given our *in vitro* findings, we hypothesized that RhoA deletion could promote axon regeneration after spinal cord injury (SCI) *in vivo*. To test this, we performed a unilateral thoracic (T) 8 dorsal hemisection in RhoANesKO mice, where RhoA is ablated in progenitor cells, which differentiate into neurons and astrocytes. Dorsal column sensory axons were traced with a unilateral sciatic nerve injection of an adeno-associated virus (AAV) expressing EGFP 14 days later, followed by perfusion of the mice after an additional 14 days (Figure 4A). We observed no difference in the extent of sensory axon regeneration between RhoANesKO mice and control WT mice (Figures 4B and 4C). Thus, RhoA deletion in the nervous system, including neurons and astrocytes, fails to promote axon regeneration after CNS injury.

Importantly, we found a striking increase in expression of the reactive astrocyte marker glial fibrillary acidic protein (GFAP) after CNS injury in RhoANesKO mice compared with WT mice by immunohistochemistry (Figure 4D) and immunoblotting (Figures 4E–4G) of lesion site extracts. Moreover, the lesion site extracts of RhoANesKO mice showed a remarkable increase in CSPGs, which are secreted by reactive astrocytes (Figures 4F and 4H). We then explored whether the enhancement in GFAP is a result of increased astrocyte density in the vicinity of the lesion site by triple immunolabeling for sex determining region Y (SRY)-box transcription factor 9 (SOX9), GFAP, and aldehyde dehydrogenase 1 family member L1 (Aldh1L1) in RhoANesKO and WT mice 2 weeks after injury (Sun et al., 2017; Zhang et al., 2014). We counted the number of SOX9-positive cells, which labels astrocytes specifically in the spinal cord, co-labeled with the astrocyte markers GFAP and Aldh1L1 to verify the staining. There was no difference in the density of lesion-site SOX9-positive astrocytes when comparing RhoANesKO and WT mice (Figures S3A and S3B), indicating that the enhancement of GFAP immunoreactivity (Figures S3A and S3C) occurred because of increased reactivity of individual astrocytes. Thus, astrocytic RhoA may regulate astrocyte reactivity and CSPG production following CNS injury.

RhoA restricts astrocyte reactivity through myosin II-mediated actin compaction but independent of microtubules

To test the possibility that RhoA regulates astrocyte-mediated inhibition of axon regeneration, we characterized cultured primary astrocytes derived from RhoANesKO mice. Immunoblot of biochemical extracts confirmed the absence of RhoA in these cells (Figure 5A). Intriguingly, RhoA ablation led to drastic

(F) Live-cell imaging of CGNs derived from WT mice grown on control substrate or CSPGs in the presence of blebbistatin or taxol. Insets show growth cones at the start of recording (0 min) as well as 1, 2, and 3 min later. An arrowhead points to the microtubule-rich central domain. Scale bar, 5 μm.

(G and H) Quantification of (F). Growth cone area (G) and dynamics (H) of WT neurons grown on control substrate (co) or CSPGs in the presence of blebbistatin or taxol. Values are plotted as mean ± SEM. * $p < 0.05$, ** $p < 0.01$ by Student's t test. n = 6 individual cell cultures, N = 96 cells.

See also Figure S2 and Video S3.

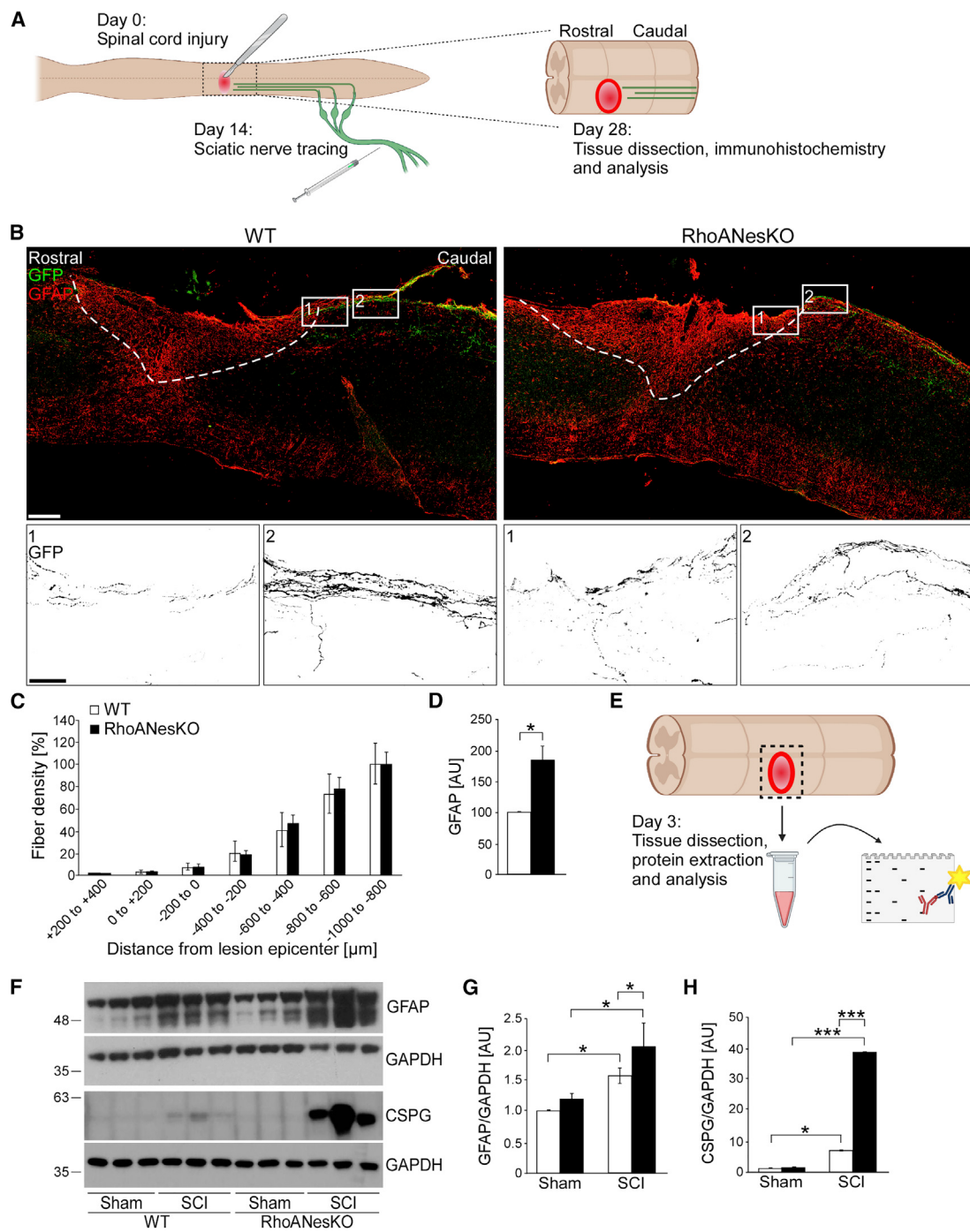


Figure 4. Simultaneous deletion of RhoA in neurons and astrocytes leads to axon regeneration failure

(A) Scheme of the timeline and methods to assess axon regeneration.

(B) Representative tile-scanned images of the spinal cord from WT and RhoANesKO mice 28 days after SCI. A fluorescent AAV-EGFP (GFP) signal and glial fibrillary acidic protein (GFAP) staining were used to visualize dorsal column fibers and reactive astrocytes marking the lesion site, respectively. Borders of the scar site are highlighted with a dashed line. Scale bar, 200 μm . Boxed areas 1 and 2 are shown in higher magnification below the overview image; scale bar, 50 μm .

(C) Quantification of regeneration in (B). Values are plotted as mean \pm SEM; n = 8 mice per group.

(D) Quantification of GFAP mean intensity in spinal cord sections in (B). Values are plotted as mean \pm SEM. *p < 0.05 by Student's t test. n = 8 animals per group.

(E) Scheme of immunoblotting of spinal cord extracts.

(legend continued on next page)

changes compared with WT astrocytes. First, we tested their migration in a scratch assay and found that RhoANesKO astrocytes, in the first 48 h after plating, migrate slightly faster than WT astrocytes (Figures S4A and S4B). Second, RhoANesKO astrocytes showed an elongated and stellate morphology, contrasting the polygonal morphology of cultured WT astrocytes (Figures 5B and 5C). Third, RhoANesKO astrocytes had decreased actin density (Figures 5B and 5D). Fourth, RhoA ablation in astrocytes increased GFAP expression (Figures 5B and 5E) and CSPG production compared with WT astrocytes (Figures 5B, 5F, S4C, and S4D). This CSPG production inhibited neurite growth because neurons contained shorter neurites when co-cultured with RhoANesKO astrocytes compared with WT astrocytes (Figures S4E and S4F), and this inhibition was neutralized upon enzymatic digestion of CSPGs by chondroitinase ABC (ChABC) (Figures S4E and S4F). Re-expression of RhoAWT in RhoANesKO astrocytes restored the polygonal morphology and GFAP expression level of WT astrocytes (Figures S4G–S4I).

Given our findings in neurons, we hypothesized that RhoA regulates astrocyte reactivity by activating myosin II to compact actin. Indeed, immunoblotting showed that phosphorylation of myosin II is downregulated in extracts of RhoANesKO astrocytes (Figures 5G and 5H). Accordingly, WT astrocytes treated with the myosin II inhibitor blebbistatin acquired a stellate morphology, reduced their F-actin content, and increased their expression of GFAP and CSPGs, displaying a phenotype similar to vehicle-treated RhoANesKO astrocytes (Figures 5B and 5I–5L). Treatment with the F-actin depolymerizing drugs latrunculin B and cytochalasin D had the same effects (Figures S5A–S5D). RhoANesKO astrocytes did not show additional changes in GFAP immunoreactivity following actin destabilization. Conversely, enforced F-actin polymerization in RhoANesKO astrocytes via treatment with the actin-polymerizing drug jasplakinolide (Bubb et al., 1994) restored their shape to a polygonal morphology and decreased GFAP expression to a level equivalent to that found in WT astrocytes (Figures 5M and 5N). Thus, RhoA impedes astrocytic GFAP expression and CSPG production by activating myosin-II mediated actin compaction.

In neurons, RhoA inhibited axon growth by activating actin compaction to restrict microtubule protrusion. We therefore wanted to find out whether RhoA restricts astrocyte reactivity through a similar mechanism. However, we found that, although stabilization of microtubules with Taxol increased microtubule density in WT and RhoANesKO astrocytes (Figures S5E and S5F), it did not affect their GFAP expression (Figures S5E and S5G) or morphology (Figures S5E and S5H). Thus, RhoA regulates astrocyte reactivity through myosin-II mediated actin compaction but independently of microtubules, which is a distinct feature of the signaling cascade we found in neurons.

RhoA activates YAP signaling in astrocytes to restrict their reactivity

We then investigated the mechanisms through which astrocytic RhoA-induced actin compaction suppresses astrocyte reactivity. Specifically, we explored the roles of serum response factor (SRF) and YAP, two key transcription factors regulated by the actin cytoskeleton. SRF transcriptional activity is inhibited by G-actin, preventing nuclear import of its coactivator myocardin-related transcription factor A (MRTD-A)/megakaryoblastic leukemia 1 (MAL) (Miralles et al., 2003). Cytochalasin D and latrunculin B depolymerize actin with opposite effects on SRF activation (Sotiropoulos et al., 1999; Vartiainen et al., 2007), but because both drugs induced features characteristic of RhoANesKO astrocytes in WT astrocytes (Figures S5A–S5D), this made the involvement of SRF unlikely. Consistently, immunocytochemistry showed no change in nuclear localization of SRF (Figures S5I and S5J). Moreover, RhoANesKO astrocytes did not restore WT characteristics upon overexpression of a constitutively active SRF mutant (SRF-VP16, hereafter called SRFca) (Figures S5K and S5L; Stern et al., 2012). Thus, RhoANesKO does not enhance astrocyte reactivity via SRF.

We then explored the role of YAP by assessing whether RhoAKO influences its nuclear translocation and activation. Remarkably, YAP localized to the cytoplasm in RhoANesKO astrocytes, contrasting its nuclear localization found in WT astrocytes (Figures S5M and S5N). Pharmacological inhibition of YAP by verteporfin or CA3 (Morce et al., 2020) caused WT astrocytes to increase GFAP expression and CSPG production (Figures 5O–5V). Thus, RhoA deletion suppresses YAP to induce GFAP expression and CSPG production in astrocytes.

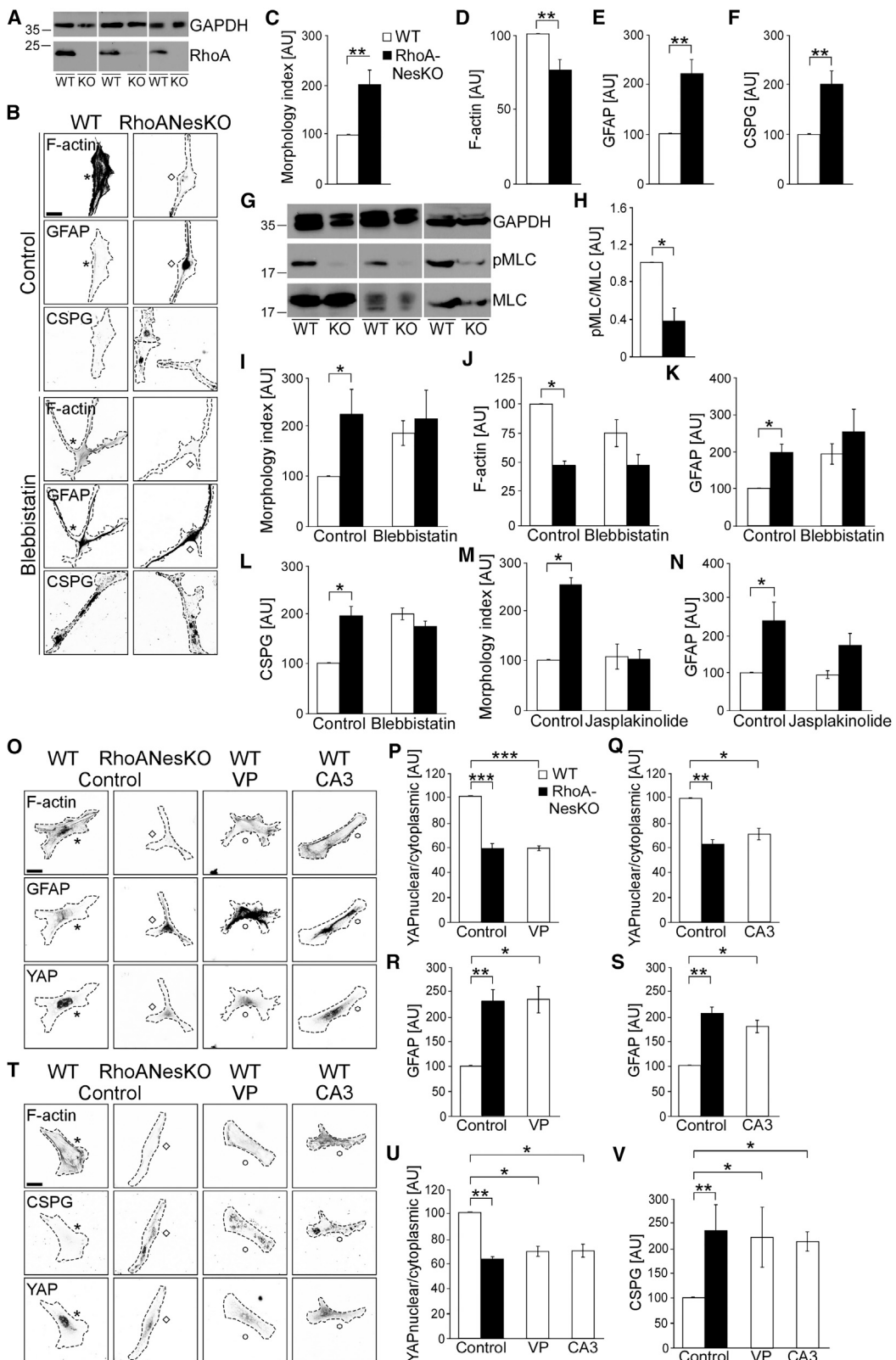
Neuron-specific RhoA deletion promotes axon regeneration after SCI

The failure of RhoANesKO to enhance axon regeneration *in vivo* could be due to enhanced inhibition of axon regeneration by RhoA-ablated astrocytes, which may abrogate a pro-regenerative effect of RhoA ablation in neurons. To test this possibility, we generated mouse lines with RhoA ablation confined to astrocytes or neurons by crossing RhoA conditional mice with mouse lines expressing Cre recombinase under control of the astrocyte-specific GFAP promoter (Gregorian et al., 2009) or the neuron-specific Synapsin I promoter (Zhu et al., 2001), respectively (Figure 6A). Both lines developed indistinguishably from WT littermates. In astrocyte-specific *gfap-cre^{tg/-}, rhoA^{f/f}* mice, hereafter called RhoAGFAPKO, biochemical extracts of the lesion site showed a similar upregulation of GFAP and CSPGs as in extracts derived from RhoANesKO mice (Figures 6B–6D). This upregulation of GFAP was not restricted to SCI but also found after brain injury (BI) to the somatosensory cortex (Figures S6A and S6B). Conversely, in neuron specific *syn-cre^{tg/-}, rhoA^{f/f}* mice, hereafter called RhoASynKO, biochemical extracts from SCI lesion sites showed no further upregulation of GFAP and CSPGs after CNS injury compared with extracts of WT mice (Figures 6E–6G).

(F) Immunoblot for GFAP and CSPGs of spinal cord extracts derived from WT and RhoANesKO mice 3 days after sham operation or SCI. GAPDH is shown as a loading control.

(G and H) Quantification of (F). For GFAP the upper band at 48 kDa, for GAPDH the band at 35 kDa, and for CSPGs the band at 63 kDa were used for quantification. Values are plotted as mean \pm SEM. * $p < 0.05$, ** $p < 0.001$ by Student's *t* test. $n = 3$ animals per group.

See also Figure S3.



(legend on next page)

To assess axon regeneration, we performed a T12 dorsal column SCI in these mice, traced the axons via sciatic nerve injection 2 weeks later, and sacrificed the mice 2 weeks after tracing. Whole-mount immunostaining and two-photon imaging of the unsectioned spinal cord (Hilton et al., 2019) demonstrated that, following astrocyte-specific RhoA deletion, dieback or retraction of sensory axons caudal to the lesion site was increased relative to WT mice (Figures 6H and 6I; Video S4). In fact, we found more “U turns” of fibers growing in the opposite direction of the lesion in RhoAGFAPKO mice relative to WT mice (Figure S6C). Thus, astrocytic RhoA deletion had an anti-regenerative effect that further restricted the growth of WT sensory axons following SCI.

Conversely, neuron-specific RhoASynKO mice showed enhanced sensory axon regeneration up to 1 mm rostral to the injury site relative to WT control mice (Figures 6H and 6J). Indeed, a proportion of RhoA-ablated neurons grew their axons through the lesion site and exhibited the irregular morphologies and trajectories characteristic of regenerating axons (Video S4; Steward et al., 2003). Thus, RhoA inactivation in neurons is pro-regenerative. As before, no difference in axon regeneration was observed in RhoANesKO mice relative to WT mice (Figures 6H and 6J). Therefore, the pro-regenerative effect of neuronal RhoA deletion is abrogated when RhoA is inactivated simultaneously in astrocytes.

Astrocyte-specific RhoA deletion causes deficits in functional recovery

As RhoA ablation in astrocytes enhanced their reactivity, which prevents axon regeneration, we hypothesized that this would hamper the recovery of function after spinal cord injury. To test this possibility, we performed a more severe injury that would enable testing of locomotor functional recovery. We performed

a contusion injury of 65 kdynes (Figures 7A and 7B) at T10 in RhoAGFAPKO, RhoASynKO, and WT mice and analyzed locomotion using the Basso mouse scale (BMS) scoring system (Basso et al., 2006). One day after injury, mice of all groups showed a BMS score of only 1, indicating slight ankle movement (Figure 7C). By 2 weeks after injury, RhoASynKO and WT mice displayed enhanced locomotor function relative to RhoAGFAPKO mice (Figure 7C). This improvement continued, with RhoASynKO and WT mice acquiring the ability to frequently or consistently plantar stepping by 42 days after injury (Figure 7C). In contrast, RhoAGFAPKO showed barely any improvement in locomotion (Figure 7C).

Subsequent immunohistochemistry analysis showed, in RhoAGFAPKO mice, besides enhanced upregulation of GFAP, an increase in lesion size volume compared with RhoASynKO and WT mice (Figures 7D and 7E). Moreover, serotonergic (5-HT) axon density in the ventral horn caudal to the injury site was reduced drastically in RhoAGFAPKO mice compared with WT mice (Figures 7F and 7G). In RhoASynKO mice, in contrast, serotonergic axon density in the ventral horn of the spinal cord was enhanced compared with WT mice (Figure 7F and 7G). However, consistent with the fact that RhoA has key functions in pre- and postsynapse formation (Antonova et al., 2001; Briz et al., 2015; Murakoshi et al., 2011), its continued genetic loss did not translate into improved functional recovery compared with WT mice (Figure 7C). Thus, astrocytic RhoA restrains scarring at the lesion site, which is a prerequisite for functional recovery.

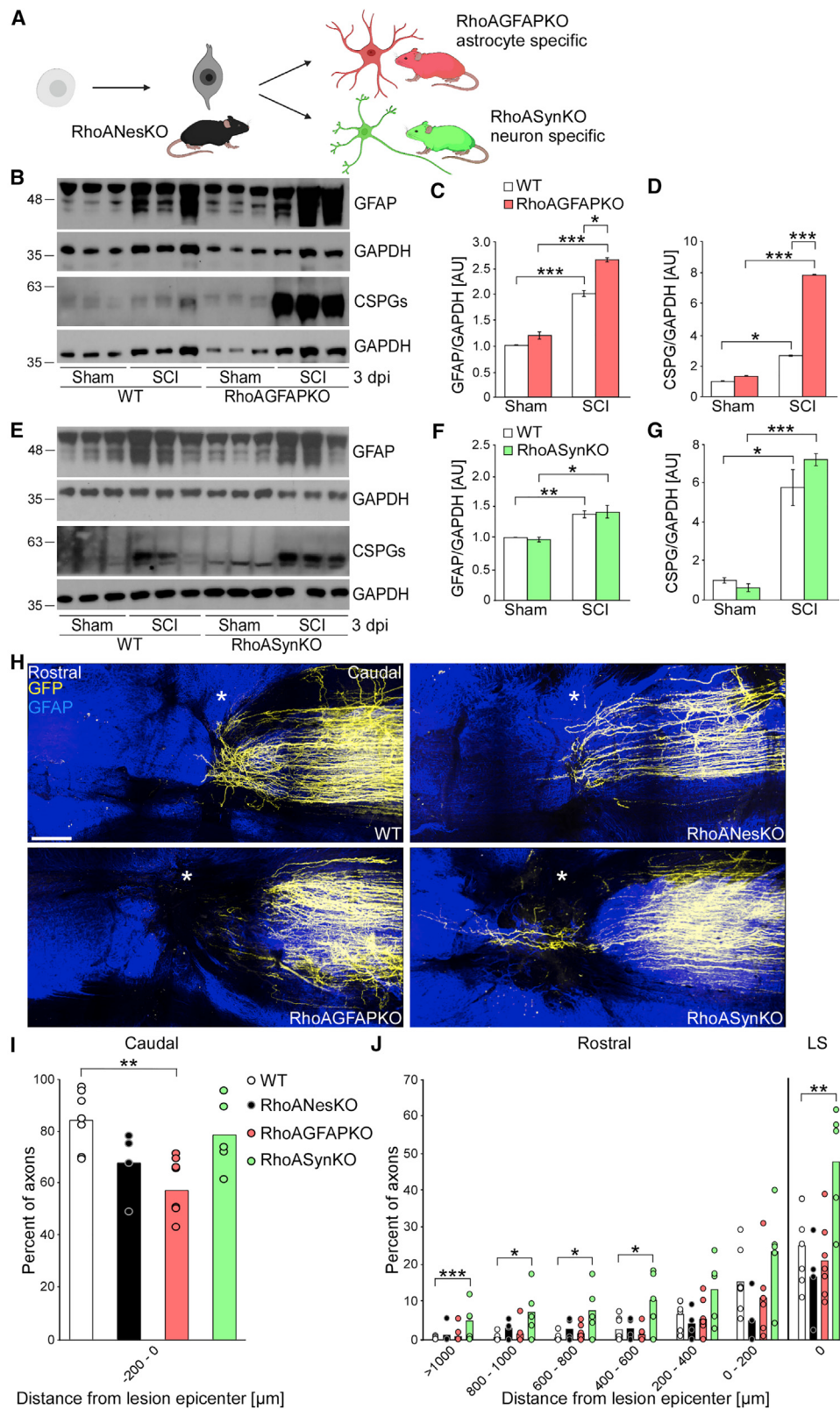
Ablation of RhoA in neurons in adult mice causes axon regeneration

In RhoASynKO mice, RhoA ablation occurs developmentally. Therefore, we investigated whether neuron-specific ablation of

Figure 5. RhoA restricts astrogliosis through myosin II and YAP signaling

- (A) Immunoblot for RhoA in WT and RhoANesKO astrocytic cell extracts. GAPDH is shown as a loading control.
- (B) Representative fluorescence images of WT and RhoANesKO astrocytes under DMSO (control) conditions or after treatment with blebbistatin and stained with phalloidin, GFAP, and CSPG antibodies. Asterisks and rhombuses indicate identical image areas. Scale bar, 10 μ m.
- (C–F) Quantifications of WT and RhoANesKO astrocytes under control conditions. Shown are morphology index (C), F-actin mean intensity (D), GFAP mean intensity (E), and CSPG mean intensity (F) of astrocytes derived from P2–P5 WT or RhoANesKO mice. Values are plotted as mean \pm SEM and normalized to the WT control. ** p < 0.01 by Student's t test. n = 5 individual cultures, N = 294 (C–E) and 252 (F) cells.
- (G) Immunoblot for MLC and pMLC in WT and RhoANesKO astrocyte extracts.
- (H) Quantification of (G). For GAPDH the lower band at 35 kDa and for pMLC and tMLC the band at 17 kDa were used for quantification. Values are plotted as mean and SEM. * p < 0.05 by Student's t test. n = 3 animals per group.
- (I–L) Quantification of WT and RhoANesKO astrocytes following treatment with blebbistatin. Shown are morphology index (I), F-actin mean intensity (J), GFAP mean intensity (K), and CSPG mean intensity (L) of astrocytes derived from WT or RhoANesKO mice under blebbistatin treatment. Values are plotted as mean \pm SEM and normalized to the WT control. * p < 0.05 by Student's t test. n = 4 individual cultures, N = 320 (I–K) and 240 (L) cells.
- (M) Morphology index of WT and RhoANesKO astrocytes following treatment with DMSO (control) or jasplakinolide. Values are plotted as mean \pm SEM and normalized to the WT control. * p < 0.05 by Student's t test. n = 4 individual cultures, N = 320 cells.
- (N) GFAP mean intensity of WT and RhoANesKO astrocytes following treatment with DMSO (control) or jasplakinolide. Values are plotted as mean \pm SEM and normalized to the WT control. * p < 0.05 by Student's t test. n = 4 individual cultures, N = 320 cells.
- (O) Representative fluorescence images of WT and RhoANesKO astrocytes under DMSO (control) conditions or after treatment with verteporfin (VP) or CA3 stained with phalloidin, GFAP, and YAP antibodies. Asterisks, rhombuses, circles, and hexagons indicate the same image areas. Scale bar, 10 μ m.
- (P–S) Quantification of (O). Shown are YAP nuclear to cytoplasmic mean intensity after VP (P) and CA3 treatment (Q) and GFAP mean intensity after VP (R) and CA3 treatment (S) in astrocytes derived from WT or RhoANesKO mice. Values are plotted as mean \pm SEM and normalized to the WT control. * p < 0.05, ** p < 0.01, *** p < 0.001 by Student's t test. n = 3 individual cultures, N = 300 cells.
- (T) Representative fluorescence images of WT and RhoANesKO astrocytes under DMSO (control) conditions or after treatment with VP or CA3 stained with phalloidin, CSPG, and YAP antibodies. Asterisks, rhombuses, circles, and hexagons indicate identical image areas. Scale bar, 10 μ m.
- (U and V) Quantification of (T). Shown are YAP nuclear to cytoplasmic mean intensity (U) and CSPG mean intensity (V) after VP and CA3 treatment of astrocytes derived from WT or RhoANesKO mice (P2–P5). Values are plotted as mean \pm SEM and normalized to the WT control. * p < 0.05, ** p < 0.01 by Student's t test. n = 4 individual cultures, N = 225 cells.

See also Figures S4 and S5.



(legend on next page)

RhoA starting in adulthood would stimulate axon regeneration (Figures 8A and 8B). To this end, we injected AAVs expressing Cre and EGFP driven by the Synapsin I promoter (Duan et al., 2020) into the sciatic nerve of adult *rhoA^{fl/fl}* mice (Figure 8A). Two weeks later, mice underwent a dorsal column lesion, as described above, and after an additional 4 weeks, animals were perfused and analyzed. We found that neuron-specific RhoA deletion in adult primary sensory neurons stimulated axon regeneration following SCI relative to control adult *rhoA^{fl/fl}* mice that were injected with AAV-GFP without Cre (Figures 8C and 8D).

Given that dorsal column axons showed such regeneration, we asked whether corticospinal axons, which are notoriously refractory to regeneration in the adult (Tuszynski and Steward, 2012), could show any sign of regeneration upon RhoA ablation. We therefore injected an AAV expressing tandem dimer (td) Tomato with or without AAV-Cre (Simpson et al., 2019) in the motor cortex of adult *rhoA^{fl/fl}* mice and performed a dorso-lateral hemisection at T12 2 weeks later and tissue clearing and 3D imaging analysis of the corticospinal tract 6 weeks after SCI (Figure 8B). As expected, RhoA deletion in adult corticospinal neurons did not stimulate their regeneration past the lesion site (Figures 8E and 8F). However, it promoted growth rostral to the injury and stimulated growth into or prevented retraction from the lesion site itself (Figures 8E and 8F). In sum, ablation of RhoA in adult neurons stimulates a regenerative response following SCI.

DISCUSSION

Here we established the physiological role of RhoA in neurons and astrocytes after CNS injury and found that neuronal and astrocytic RhoA functions have opposing consequences on axon regeneration. Neuronal RhoA restricts axon regeneration by linking inhibitory extracellular signaling to a core process in neurons that controls their polarization during development. CNS myelin and scar-derived factors converge on RhoA activation, which induces myosin II-mediated actin compaction in the growth cone, preventing microtubule protrusion. Astrocytic RhoA controls injury-induced astrogliosis and CSPG production through myosin II but independent of microtubules. Only neuron-specific RhoA ablation promotes regeneration because astrocytic ablation of RhoA is anti-regenerative. This work demonstrates the importance of cell-type-specific RhoA targeting

or manipulating a distinct downstream process to minimize side effects. It also highlights the need for a detailed understanding of the cell biology to tailor potential clinically relevant approaches.

Controlling axon regeneration: From extracellular inhibitory factors down to the effector

RhoA has been proposed to be a point of convergence that transduces extracellular inhibition to intracellular processes to limit axon regeneration. However, even though numerous RhoA downstream effectors have been identified (Fujita and Yamashita, 2014; Sami et al., 2020), the physiologically relevant effectors have remained unclear. Here we deciphered how neuronal RhoA relays extracellular inhibitory signaling to prevent axon regeneration by acting on the cytoskeleton. Extracellularly, myelin-associated inhibitors and CSPGs signal through their receptors to RhoA (Fujita and Yamashita, 2014; Hu and Selzer, 2017), which prevents microtubule protrusion through actomyosin-mediated inhibition. In fact, our data highlight that subcortical actin becomes condensed upon exposure to CSPGs, which is RhoA dependent.

Therefore, ablation of RhoA in neurons allows axon regeneration through a defined cellular cascade that ultimately enables microtubule protrusion in the axon tip, propelling it forward (Dupraz et al., 2019; Santos et al., 2020). Thus, RhoA interconnects extracellular inhibitory signals to microtubules, whose pharmacological stabilization through Taxol and epothilones has beneficial effects after CNS injury (Ertürk et al., 2007; Hellal et al., 2011; Kondo et al., 2019; Kugler et al., 2020; Nagai et al., 2016; Ruschel and Bradke, 2018; Ruschel et al., 2015; Sandner et al., 2018; Zhao et al., 2017).

Even though RhoA is a key mediator of axon growth inhibition, additional intracellular mediators of outgrowth inhibition are involved. For example, we found that CSPGs induce cofilin inactivation independent of RhoA signaling, and cofilin is necessary and sufficient to induce axon regeneration in the injured CNS (Tedeschi et al., 2019). Given that RhoA ablation and cofilin overexpression have additive effects on neurite growth in culture, it is possible that manipulating both pathways concurrently will lead to more pronounced axon regeneration than each manipulation alone.

Aside from the cytoskeleton, it will be essential to understand how extracellular growth inhibitors influence other downstream mediators that dictate regenerative fate, including protein

Figure 6. Neuronal deletion of RhoA promotes regeneration, whereas astrocytic deletion of RhoA abrogates regeneration

- (A) Overview of the transgenic mice used in the experiment.
 - (B) Immunoblot for GFAP and CSPGs in spinal cord extracts from WT and RhoAGFAPKO mice with or without SCI. GAPDH is shown as a loading control.
 - (C and D) Quantification of (B). For GFAP the upper band at 48 kDa, for GAPDH the band at 35 kDa, and for CSPG the band at 63 kDa were used for quantification. Values are plotted as mean and SEM and normalized to the WT control. *p < 0.05, **p < 0.001 by Student's t test. n = 3 individual animals.
 - (E) Immunoblot for GFAP and CSPGs in spinal cord extracts from WT and RhoASynKO mice with or without SCI. GAPDH is shown as a loading control.
 - (F and G) Quantification of (E). *p < 0.05, **p < 0.01, ***p < 0.001 by Student's t test. n = 3 individual animals.
 - (H) 3D rendering of tile scan imaged dorsal column sensory axons labeled with GFP in whole-mount spinal cord immunostained with GFAP antibody 4 weeks after SCI. Asterisks indicate lesion centers. The GFAP signal was set to saturating levels to outline the lesion. Scale bar, 200 μm.
 - (I) Quantification of axon density caudal to the lesion site. **p < 0.01 by one-way ANOVA, followed by permutation test. WT, n = 7; RhoANesKO, n = 4; RhoAGFAPKO, n = 7; RhoASynKO, n = 5.
 - (J) Quantification of axon density rostral to the lesion site and at the lesion site (LS); scatterplot with mean. *p < 0.05, **p < 0.01, ***p < 0.001 by permutation test. WT, n = 7; RhoANesKO, n = 4; RhoAGFAPKO; n = 7; RhoASynKO, n = 5.
- See also Figure S6 and Video S4.

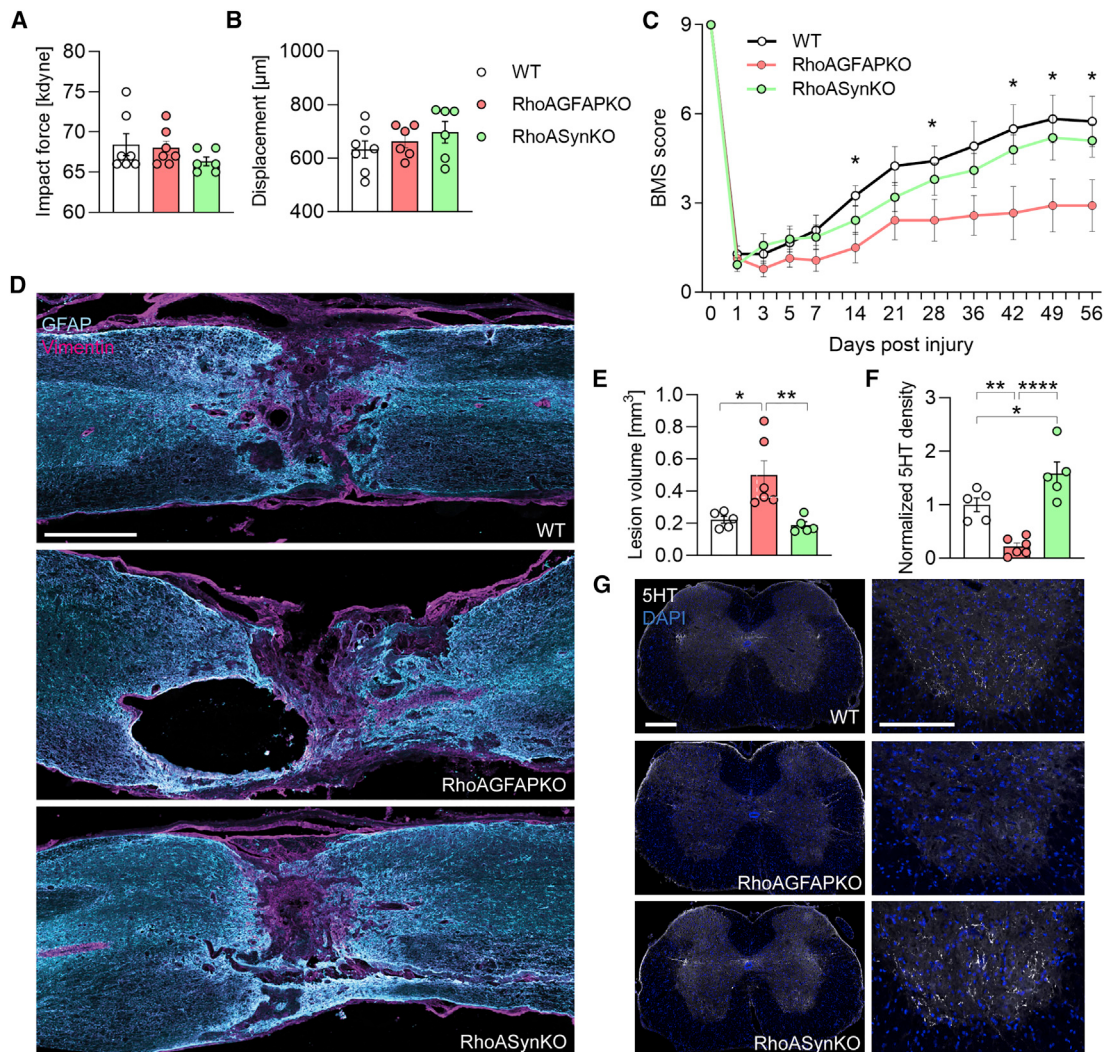


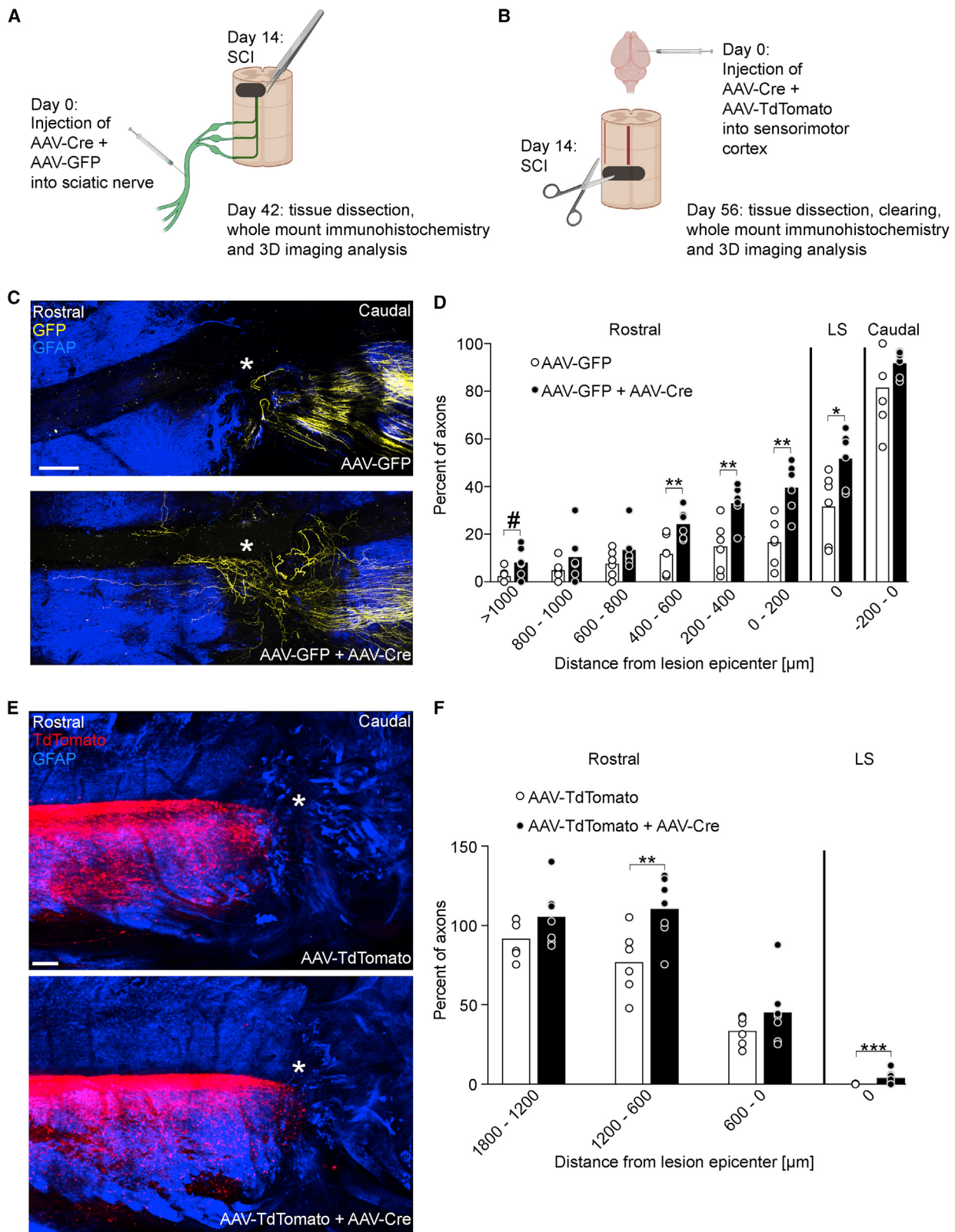
Figure 7. Astrocytic RhoA ablation restricts locomotor recovery following SCI

(A and B) Impact force (A) and displacement (B) in WT, RhoAGFAPKO, and RhoASynKO mice in generation of spinal cord contusion injury.
(C) Time course of locomotor function evaluated by open field BMS. $F_{2,18} = 3.904$, $p = 0.031$ by mixed effects model followed by Fisher's LSD, * $p < 0.05$ RhoAGFAPKO versus WT. WT, $n = 7$; RhoAGFAPKO, $n = 6$; RhoASynKO, $n = 6$ mice.
(D) Representative fluorescence images of WT, RhoAGFAPKO, and RhoASynKO sagittal sections of SCI lesion sites (LSs) 8 weeks after injury and stained with GFAP and Vimentin antibodies. Scale bar, 500 μ m.
(E) Lesion volume in WT, RhoAGFAPKO, and RhoASynKO mice 8 weeks after contusion SCI. * $p < 0.05$, ** $p < 0.01$ by one-way ANOVA followed by Bonferroni's post-test. WT, $n = 5$; RhoAGFAPKO, $n = 6$; RhoASynKO, $n = 5$ mice.
(F) Serotonin (5-HT) density in the ventral horns of lumbar spinal cords in WT, RhoAGFAPKO, and RhoASynKO mice normalized to the mean value in WT mice. * $p < 0.05$, ** $p < 0.01$, *** $p < 0.0001$ by one-way ANOVA followed by Bonferroni's post-test. WT, $n = 5$; RhoAGFAPKO, $n = 6$; RhoASynKO, $n = 5$.
(G) Representative fluorescence images of WT, RhoAGFAPKO, and RhoASynKO coronal sections of the lumbar spinal cord caudal to SCI and stained with 5-HT antibody as well as DAPI. Scale bar, 200 μ m. Insets on the right of each image show the ventral horn. Scale bar, 100 μ m.

translation (Lindner et al., 2013), mitochondrial dynamics (Smith and Gallo, 2018), membrane trafficking (Bloom and Morgan, 2011), and the inflammatory response contributing to secondary injury (Gonzalez et al., 2003). Indeed, RhoA might also have an anti-inflammatory effect; there is evidence that RhoA suppresses microglia activation in different CNS pathology models (Ding et al., 2010; Hendriks et al., 2004; Tönges et al., 2014) as well as release of pro-inflammatory cytokines after SCI (McKerracher and Anderson, 2013).

Astrocytic RhoA regulates astrocyte reactivity and CSPG production

The role of astrocytes in axon regeneration is under debate. Historically, reactive astrocytes have been considered a barrier to regeneration because of their density surrounding the lesion site and association with CSPGs (Filios and Silver, 2016; Liuzzi and Lasek, 1987; McKeon et al., 1991, 1999). However, in certain functions, reactive astrocytes are pro-regenerative. For example, they sequester fibrotic and inflammatory cells to a non-neuronal lesion



(legend on next page)

core, restricting expansion of cells that are potently inhibitory to axon growth (Sabelström et al., 2013; Sofroniew, 2005). Some molecular manipulations of reactive astrocytes, including leucine zipper-bearing kinase overexpression, can further reduce the size of the inhibitory non-neuronal lesion core concurrently with increased expression of GFAP, demonstrating the importance of astrocyte reactivity in this process (Chen et al., 2018). More recently, it has been concluded that astrocytes are permissive for regenerating axons based on the following reasons. First, genetic removal of astrocytes, even in chronic injury, fails to induce axon regeneration and enhances axon retraction from a SCI lesion site (Anderson et al., 2016). Second, reactive astrocytes express growth-promoting molecules and sequester growth-inhibitory cells (Anderson et al., 2016). Thus, reactive astrocytes clearly have growth-promoting roles after CNS injury. However, their ablation may enhance infiltration of other inhibitory cell types and exacerbate inhibitory CSPG production by non-astrocytes after SCI (Anderson et al., 2016; Bradbury and Burnside, 2019). Therefore, it has remained unclear whether astrocytes can directly inhibit axon growth after CNS injury.

Here, by identifying RhoA as a regulator of astrocyte reactivity and CSPG production, our work demonstrates that, by secreting CSPGs, reactive astrocytes inhibit axon growth. This anti-regenerative function of astrocytes, uncovered by genetic ablation of RhoA, is an important benchmark to clarify their role during CNS injury. It will be interesting to decipher whether the pro-regenerative and anti-regenerative functions of astrocytes in axon regeneration are carried out by cells differing in their reactive states (Liddelow and Barres, 2017) or whether they arise in response to different extracellular cues (Hara et al., 2017).

The intracellular mechanisms orchestrating the astrocyte response to injury are largely unclear (Yu et al., 2020). Here we found that the actin cytoskeleton critically regulates astrocyte reactivity. Specifically, ablation of RhoA in astrocytes increased astrocyte reactivity by diminishing myosin II-mediated actin compaction. This inactivates YAP signaling, resulting in increased GFAP and CSPG expression. However, unlike in neurons, actin acts independent of microtubules in this process. Consistent with this, moderate microtubule stabilization by Taxol mimics ablation of RhoA in neurons in enhancing regeneration but does not influence astrocyte reactivity (Hellal et al., 2011), suggesting that microtubules play only a minor role in defining astrocyte reactivity.

Cell-targeting strategies: Perspective for axon regeneration therapies based on RhoA

The promising effects of RhoA inactivation by C3 exoenzyme in rodent models of SCI (Ellezam et al., 2002) triggered immense research efforts and led to clinical trials (Fehlings et al., 2011, 2018). Although the phase II trial was discontinued after lack of

efficacy found in an interim analysis (Fehlings et al., 2021), our data highlight the hurdles clinical trials encounter when the underlying cellular mechanisms of a potential treatment in a complex cellular environment are unclear. In fact, our data warrant further investigation of RhoA as a therapeutic target. RhoA, however, needs to be manipulated with caution in the injured human spinal cord, given its regulation of astrocyte reactivity. Different strategies might overcome this issue. Manipulation of RhoA should be as specific to neurons as possible to avoid a negative influence on other cell types (Socodato et al., 2020). This could be achieved by neuron-specific targeting of the RhoA gene itself or through gene therapy approaches using the appropriate combination of capsid serotype and target gene promotor (Blessing and Déglon, 2016; Shevtsova et al., 2005). However, it may be necessary to bring back RhoA function when synapse formation takes place, as our functional recovery data suggest. Hence, a transient inactivation approach may be more helpful. It may be promising to transiently and pharmacologically manipulate the signaling cascade downstream of RhoA, where astrocytes are less influenced. We showed, for example, that microtubule stabilization mimics the positive effect of RhoA ablation in neurons without the negative effect of RhoA ablation in astrocytes. Thus, the RhoA signaling cascade is central for neural repair when manipulated appropriately.

Conclusions

Our work provides a missing link between extracellular inhibitory factors and the physiological effectors restraining axon regeneration after CNS injury. CNS myelin factors and CSPGs activate neuronal RhoA, which, in turn, activates myosin II to condense actin filaments. This mechanism restrains microtubule protrusion and, thereby, axon regrowth in the lesioned CNS. By similar actin-based mechanisms but independent of microtubules and by regulating YAP signaling, RhoA restricts astrocyclic reactivity following CNS injury. By cell-type-specific genetic ablation in combination with SCI studies, we provide evidence that reactive astrocytes are anti-regenerative. Consequently, RhoA signaling is a double-edged sword in spinal cord regeneration, with opposing consequences in neurons and astrocytes. Hence, the full regenerative potential of the RhoA signaling pathway can be exploited by cell-type-specific manipulation of this pathway or by directing downstream effectors that lack astrogliosis-promoting activity.

STAR★METHODS

Detailed methods are provided in the online version of this paper and include the following:

- KEY RESOURCES TABLE

Figure 8. Neuronal RhoA ablation in adulthood promotes sensory axon regeneration and corticospinal axon growth following SCI

(A and B). Schematics of the experimental paradigms to assess sensory (A) and corticospinal (B) axon regeneration in adult *rhoA^{f/f}* mice after spinal cord injury (SCI). (C) 3D rendering of tile scan imaged dorsal column sensory axons labeled with AAV-EGFP in spinal cord immunostained with GFAP antibody 4 weeks after SCI. Asterisks indicate lesion centers. Scale bar, 200 μ m.
(D) Quantification of axon regeneration in (C). #p < 0.10, *p < 0.05, **p < 0.01 by permutation test; n = 6 animals per group.
(E) 3D rendering of tile scan imaged corticospinal axons labeled with TdTomato in whole-mount spinal cord immunostained with GFAP antibody and cleared 6 weeks after SCI. Asterisks indicate lesion centers. Scale bar, 200 μ m.
(F) Quantification of axon density rostral to the LS in (E). **p < 0.01, ***p < 0.001 by permutation test. AAV-TdTomato, n = 6; AAV-TdTomato + AAV-Cre, n = 7.

- RESOURCE AVAILABILITY
 - Lead contact
 - Materials availability
 - Data and code availability
- EXPERIMENTAL MODEL AND SUBJECT DETAILS
 - Animals
- METHOD DETAILS
 - Primary cell culture
 - Immunocytochemistry
 - Live cell microscopy
 - Scratch assay
 - Co-culture of astrocytes and CGNs
 - Immunoblotting
 - F- to G-actin ratio assay
 - Brain injury
 - Fiber tracing
 - Spinal Cord Injury (SCI)
 - Functional assessment
 - Tissue Processing Sectioned Tissue Analyses
 - Tissue Processing Whole Mount Spinal Cords
 - Microscopy and Image Analysis
- QUANTIFICATION AND STATISTICAL ANALYSIS

SUPPLEMENTAL INFORMATION

Supplemental information can be found online at <https://doi.org/10.1016/j.neuron.2021.08.014>.

ACKNOWLEDGMENTS

We thank A. Kania, T. Misgeld, K.A. Nave, T. Pietralla, B. Schaffran, G. Tavosanis, A. Husch, and R. Wedlich-Söldner for critically reading and discussing the manuscript; G. Posern, D. Schmucker, K. Flynn, and G. Edwards-Faret for scientific discussions; and B. Knöll for the SRF-VP16 plasmid. We are grateful to the Animal Research Facility, the Light Microscope Facility, and the Image and Data Analysis Facility of the DZNE Bonn. The latter designed the script for the permutation test analysis that was executed by B. Schaffran. We are indebted to B. Randel, A.-T. Pham, L. Meyn, S. Weber, and K. Weisheit for technical assistance. We also want to thank all members of the F.B. laboratory for productive discussions related to this project. This work was supported by Deutsche Forschungsgesellschaft (DFG) (to S.S. and F.B.), the International Foundation for Research in Paraplegia (IRP) (to F.B.), and Wings for Life (to B.J.H. and F.B.). F.B. is a member of the excellence cluster ImmunoSensation2 and the SFBs 1089 and 1158 and a recipient of the Roger De Spoelberch Prize.

AUTHOR CONTRIBUTIONS

S.S. and F.B. conceived the project. S.S., B.J.H., E.R.B., and F.B. designed the research. S.S., B.J.H., E.R.B., S.D., E.E.H., and J.M.G. performed the research. S.S., B.J.H., E.R.B., and S.D. analyzed the data. C.B. provided the mutant mice. F.B. supervised the research. S.S., B.J.H., and F.B. wrote the paper.

DECLARATION OF INTERESTS

H. Witte, A. Ertürk, F. Hellal, and F.B. filed a patent on the use of microtubule-stabilizing compounds for the treatment of lesions of CNS axons (European Patent 1858498, European patent application EP 11 00 9155.0, U.S. patent application 11/908,118).

Received: February 12, 2021

Revised: July 16, 2021

Accepted: August 11, 2021

Published: September 10, 2021

REFERENCES

- Anderson, M.A., Burda, J.E., Ren, Y., Ao, Y., O'Shea, T.M., Kawaguchi, R., Coppola, G., Khakh, B.S., Deming, T.J., and Sofroniew, M.V. (2016). Astrocyte scar formation aids central nervous system axon regeneration. *Nature* 532, 195–200.
- Anderson, M.A., O'Shea, T.M., Burda, J.E., Ao, Y., Barlatey, S.L., Bernstein, A.M., Kim, J.H., James, N.D., Rogers, A., Kato, B., et al. (2018). Required growth facilitators propel axon regeneration across complete spinal cord injury. *Nature* 561, 396–400.
- Antonova, I., Arancio, O., Trillat, A.C., Wang, H.G., Zablow, L., Udo, H., Kandel, E.R., and Hawkins, R.D. (2001). Rapid increase in clusters of presynaptic proteins at onset of long-lasting potentiation. *Science* 294, 1547–1550.
- Basso, M.D., Fisher, L.C., Anderson, A.J., Jakeman, L.B., McTigue, D.M., and Popovich, P.G. (2006). Basso Mouse Scale for locomotion detects differences in recovery after spinal cord injury in five common mouse strains. *J Neurotrauma* 23 (5), 635–659. <https://doi.org/10.1089/neu.2006.23.635>.
- Beach, J.R., Licate, L.S., Crish, J.F., and Egelhoff, T.T. (2011). Analysis of the role of Ser1/Ser2/Thr9 phosphorylation on myosin II assembly and function in live cells. *BMC Cell Biol.* 12, 52.
- Bentley, D., and Toroian-Raymond, A. (1986). Disoriented pathfinding by pioneer neurone growth cones deprived of filopodia by cytochalasin treatment. *Nature* 323, 712–715.
- Blanquie, O., and Bradke, F. (2018). Cytoskeleton dynamics in axon regeneration. *Curr. Opin. Neurobiol.* 51, 60–69.
- Blessing, D., and Déglon, N. (2016). Adeno-associated virus and lentivirus vectors: a refined toolkit for the central nervous system. *Curr. Opin. Virol.* 21, 61–66.
- Bloom, O.E., and Morgan, J.R. (2011). Membrane trafficking events underlying axon repair, growth, and regeneration. *Mol. Cell. Neurosci.* 48, 339–348.
- Boevid, M.J., Mikdache, A., Lesport, E., Degerny, C., and Tawk, M. (2020). Rho GTPases Signaling in Zebrafish Development and Disease. *Cells* 9, 2634.
- Bradbury, E.J., and Burnside, E.R. (2019). Moving beyond the glial scar for spinal cord repair. *Nat. Commun.* 10, 3879.
- Bradke, F., and Dotti, C.G. (1999). The role of local actin instability in axon formation. *Science* 283, 1931–1934.
- Briz, V., Zhu, G., Wang, Y., Liu, Y., Avetisyan, M., Bi, X., and Baudry, M. (2015). Activity-dependent rapid local RhoA synthesis is required for hippocampal synaptic plasticity. *J. Neurosci.* 35, 2269–2282.
- Bubb, M.R., Senderowicz, A.M., Sausville, E.A., Duncan, K.L., and Korn, E.D. (1994). Jasplakinolide, a cytotoxic natural product, induces actin polymerization and competitively inhibits the binding of phalloidin to F-actin. *J. Biol. Chem.* 269, 14869–14871.
- Burda, J.E., and Sofroniew, M.V. (2014). Reactive gliosis and the multicellular response to CNS damage and disease. *Neuron* 81, 229–248.
- Chan, C.C., Wong, A.K., Liu, J., Steeves, J.D., and Tetzlaff, W. (2007). ROCK inhibition with Y27632 activates astrocytes and increases their expression of neurite growth-inhibitory chondroitin sulfate proteoglycans. *Glia* 55, 369–384.
- Chen, M., Geoffroy, C.G., Meves, J.M., Narang, A., Li, Y., Nguyen, M.T., Khai, V.S., Kong, X., Steinke, C.L., Carolino, K.I., et al. (2018). Leucine Zipper-Bearing Kinase Is a Critical Regulator of Astrocyte Reactivity in the Adult Mammalian CNS. *Cell Rep.* 22, 3587–3597.
- Chia, J.X., Efimova, N., and Svitkina, T.M. (2016). Neurite outgrowth is driven by actin polymerization even in the presence of actin polymerization inhibitors. *Mol. Biol. Cell*, mbc.E16-04-0253.
- Coles, C.H., and Bradke, F. (2015). Coordinating neuronal actin-microtubule dynamics. *Curr. Biol.* 25, R677–R691.
- Cregg, J.M., DePaul, M.A., Filous, A.R., Lang, B.T., Tran, A., and Silver, J. (2014). Functional regeneration beyond the glial scar. *Exp. Neurol.* 253, 197–207.

- Curcio, M., and Bradke, F. (2018). Axon Regeneration in the Central Nervous System: Facing the Challenges from the Inside. *Annu. Rev. Cell Dev. Biol.* 34, 495–521.
- DeBellard, M.E., Tang, S., Mukhopadhyay, G., Shen, Y.J., and Filbin, M.T. (1996). Myelin-associated glycoprotein inhibits axonal regeneration from a variety of neurons via interaction with a sialoglycoprotein. *Mol. Cell. Neurosci.* 7, 89–101.
- Dent, E.W., Gupton, S.L., and Gertler, F.B. (2011). The growth cone cytoskeleton in axon outgrowth and guidance. *Cold Spring Harb. Perspect. Biol.* 3, a001800.
- Dergham, P., Ellezam, B., Essagian, C., Avedissian, H., Lubell, W.D., and McKerracher, L. (2002). Rho signaling pathway targeted to promote spinal cord repair. *J. Neurosci.* 22, 6570–6577.
- Ding, J., Li, Q.Y., Wang, X., Sun, C.H., Lu, C.Z., and Xiao, B.G. (2010). Fasudil protects hippocampal neurons against hypoxia-reoxygenation injury by suppressing microglial inflammatory responses in mice. *J. Neurochem.* 114, 1619–1629.
- Duan, Z.R.S., Che, A., Chu, P., Modol, L., Bollmann, Y., Babij, R., Fethcho, R.N., Otsuka, T., Fuccillo, M.V., Liston, C., et al. (2020). GABAergic Restriction of Network Dynamics Regulates Interneuron Survival in the Developing Cortex. *Neuron* 105, 75–92.e5.
- Duffy, P., Schmandke, A., Schmandke, A., Sigworth, J., Narumiya, S., Cafferty, W.B., and Strittmatter, S.M. (2009). Rho-associated kinase II (ROCKII) limits axonal growth after trauma within the adult mouse spinal cord. *J. Neurosci.* 29, 15266–15276.
- Dupraz, S., Hilton, B.J., Husch, A., Santos, T.E., Coles, C.H., Stern, S., Brakebusch, C., and Bradke, F. (2019). RhoA Controls Axon Extension Independent of Specification in the Developing Brain. *Curr. Biol.* 29, 3874–3886.e9.
- Ellezam, B., Dubreuil, C., Winton, M., Loy, L., Dergham, P., Sellés-Navarro, I., and McKerracher, L. (2002). Inactivation of intracellular Rho to stimulate axon growth and regeneration. *Prog. Brain Res.* 137, 371–380.
- Ertürk, A., Hellal, F., Enes, J., and Bradke, F. (2007). Disorganized microtubules underlie the formation of retraction bulbs and the failure of axonal regeneration. *J. Neurosci.* 27, 9169–9180.
- Fehlings, M.G., Theodore, N., Harrop, J., Maurais, G., Kuntz, C., Shaffrey, C.I., Kwon, B.K., Chapman, J., Yee, A., Tighe, A., and McKerracher, L. (2011). A phase I/II clinical trial of a recombinant Rho protein antagonist in acute spinal cord injury. *J. Neurotrauma* 28, 787–796.
- Fehlings, M.G., Kim, K.D., Aarabi, B., Rizzo, M., Bond, L.M., McKerracher, L., Vaccaro, A.R., and Okonkwo, D.O. (2018). Rho Inhibitor VX-210 in Acute Traumatic Subaxial Cervical Spinal Cord Injury: Design of the SPInal Cord Injury Rho INhibition InvestiGation (SPRING) Clinical Trial. *J. Neurotrauma* 35, 1049–1056.
- Fehlings, M.G., Chen, Y., Aarabi, B., Ahmad, F., Anderson, K.D., Dumont, T., Fournier, D.R., Harrop, J.S., Kim, K.D., and Kwon, B.K. (2021). A Randomized Controlled Trial of Local Delivery of a Rho Inhibitor (VX-210) in Patients with Acute Traumatic Cervical Spinal Cord Injury. *J. Neurotrauma* 38, 2065–2072.
- Filous, A.R., and Silver, J. (2016). “Targeting astrocytes in CNS injury and disease: A translational research approach”. *Prog. Neurobiol.* 144, 173–187.
- Flynn, K.C., Hellal, F., Neukirchen, D., Jacob, S., Tahirovic, S., Dupraz, S., Stern, S., Garvalov, B.K., Gurniak, C., Shaw, A.E., et al. (2012). ADF/cofilin-mediated actin retrograde flow directs neurite formation in the developing brain. *Neuron* 76, 1091–1107.
- Fujita, Y., and Yamashita, T. (2014). Axon growth inhibition by RhoA/ROCK in the central nervous system. *Front. Neurosci.* 8, 338.
- Geoffroy, C.G., and Zheng, B. (2014). Myelin-associated inhibitors in axonal growth after CNS injury. *Curr. Opin. Neurobiol.* 27, 31–38.
- Gomez, T.M., and Letourneau, P.C. (2014). Actin dynamics in growth cone motility and navigation. *J. Neurochem.* 129, 221–234.
- Gonzalez, R., Glaser, J., Liu, M.T., Lane, T.E., and Keirstead, H.S. (2003). Reducing inflammation decreases secondary degeneration and functional deficit after spinal cord injury. *Exp. Neurol.* 184, 456–463.
- Gregorian, C., Nakashima, J., Le Belle, J., Ohab, J., Kim, R., Liu, A., Smith, K.B., Groszer, M., Garcia, A.D., Sofroniew, M.V., et al. (2009). Pten deletion in adult neural stem/progenitor cells enhances constitutive neurogenesis. *J. Neurosci.* 29, 1874–1886.
- Griffin, J.M., and Bradke, F. (2020). Therapeutic repair for spinal cord injury: combinatory approaches to address a multifaceted problem. *EMBO Mol. Med.* 12, e11505.
- Hara, M., Kobayakawa, K., Ohkawa, Y., Kumamaru, H., Yokota, K., Saito, T., Kijima, K., Yoshizaki, S., Harimaya, K., Nakashima, Y., and Okada, S. (2017). Interaction of reactive astrocytes with type I collagen induces astrocystic scar formation through the integrin-N-cadherin pathway after spinal cord injury. *Nat. Med.* 23, 818–828.
- He, Z., and Jin, Y. (2016). Intrinsic Control of Axon Regeneration. *Neuron* 90, 437–451.
- He, M., Ding, Y., Chu, C., Tang, J., Xiao, Q., and Luo, Z.G. (2016). Autophagy induction stabilizes microtubules and promotes axon regeneration after spinal cord injury. *Proc. Natl. Acad. Sci. USA* 113, 11324–11329.
- Hellal, F., Hurtado, A., Ruschel, J., Flynn, K.C., Laskowski, C.J., Umlauf, M., Kapitein, L.C., Strikis, D., Lemmon, V., Bixby, J., et al. (2011). Microtubule stabilization reduces scarring and causes axon regeneration after spinal cord injury. *Science* 331, 928–931.
- Hendriks, J.J., Alblas, J., van der Pol, S.M., van Tol, E.A., Dijkstra, C.D., and de Vries, H.E. (2004). Flavonoids influence monocytic GTPase activity and are protective in experimental allergic encephalitis. *J. Exp. Med.* 200, 1667–1672.
- Hilton, B.J., and Bradke, F. (2017). Can injured adult CNS axons regenerate by recapitulating development? *Development* 144, 3417–3429.
- Hilton, B.J., Blanque, O., Tedeschi, A., and Bradke, F. (2019). High-resolution 3D imaging and analysis of axon regeneration in unsectioned spinal cord with or without tissue clearing. *Nat. Protoc.* 14, 1235–1260.
- Hu, J., and Selzer, M.E. (2017). RhoA as a target to promote neuronal survival and axon regeneration. *Neural Regen. Res.* 12, 525–528.
- Hur, E.M., Yang, I.H., Kim, D.H., Byun, J., Saijilafu, Xu, W.L., Nicovich, P.R., Cheong, R., Levchenko, A., Thakor, N., and Zhou, F.Q. (2011). Engineering neuronal growth cones to promote axon regeneration over inhibitory molecules. *Proc. Natl. Acad. Sci. USA* 108, 5057–5062.
- Jackson, B., Peyrollier, K., Pedersen, E., Basse, A., Karlsson, R., Wang, Z., Lefever, T., Ochsenebein, A.M., Schmidt, G., Aktories, K., et al. (2011). RhoA is dispensable for skin development, but crucial for contraction and directed migration of keratinocytes. *Mol. Biol. Cell* 22, 593–605.
- Jones, S.L., Selzer, M.E., and Gallo, G. (2006). Developmental regulation of sensory axon regeneration in the absence of growth cones. *J. Neurobiol.* 66, 1630–1645.
- Kondo, S., Takahashi, K., Kinoshita, Y., Nagai, J., Wakatsuki, S., Araki, T., Goshima, Y., and Ohshima, T. (2019). Genetic inhibition of CRMP2 phosphorylation at serine 522 promotes axonal regeneration after optic nerve injury. *Sci. Rep.* 9, 7188.
- Kugler, C., Thielscher, C., Tambe, B.A., Schwarz, M.K., Halle, A., Bradke, F., and Petzold, G.C. (2020). Epothilones Improve Axonal Growth and Motor Outcomes after Stroke in the Adult Mammalian CNS. *Cell Rep. Med.* 1, 100159.
- Kunda, P., Paglini, G., Quiroga, S., Kosik, K., and Caceres, A. (2001). Evidence for the involvement of Tiam1 in axon formation. *J. Neurosci.* 21, 2361–2372.
- Lehmann, M., Fournier, A., Selles-Navarro, I., Dergham, P., Sebok, A., Leclerc, N., Tigyi, G., and McKerracher, L. (1999). Inactivation of Rho signaling pathway promotes CNS axon regeneration. *J. Neurosci.* 19, 7537–7547.
- Liddelow, S.A., and Barres, B.A. (2017). Reactive Astrocytes: Production, Function, and Therapeutic Potential. *Immunity* 46, 957–967.
- Lindner, R., Puttagunta, R., and Di Giovanni, S. (2013). Epigenetic regulation of axon outgrowth and regeneration in CNS injury: the first steps forward. *Neurotherapeutics* 10, 771–781.

- Liu, R.Y., and Snider, W.D. (2001). Different signaling pathways mediate regenerative versus developmental sensory axon growth. *J. Neurosci.* 21, RC164.
- Liuzzi, F.J., and Lasek, R.J. (1987). Astrocytes block axonal regeneration in mammals by activating the physiological stop pathway. *Science* 237, 642–645.
- Luo, L. (2000). Rho GTPases in neuronal morphogenesis. *Nat. Rev. Neurosci.* 1, 173–180.
- McKeon, R.J., Schreiber, R.C., Rudge, J.S., and Silver, J. (1991). Reduction of neurite outgrowth in a model of glial scarring following CNS injury is correlated with the expression of inhibitory molecules on reactive astrocytes. *J. Neurosci.* 11, 3398–3411.
- McKeon, R.J., Juryne, M.J., and Buck, C.R. (1999). The chondroitin sulfate proteoglycans neurocan and phosphacan are expressed by reactive astrocytes in the chronic CNS glial scar. *J. Neurosci.* 19, 10778–10788.
- McKerracher, L., and Anderson, K.D. (2013). Analysis of recruitment and outcomes in the phase I/IIa Cethrin clinical trial for acute spinal cord injury. *J. Neurotrauma* 30, 1795–1804.
- Miralles, F., Posern, G., Zaromytidou, A.I., and Treisman, R. (2003). Actin dynamics control SRF activity by regulation of its coactivator MAL. *Cell* 113, 329–342.
- Morice, S., Mullard, M., Brion, R., Dupuy, M., Renault, S., Tesfaye, R., Brounais-Le Royer, B., Ory, B., Redini, F., and Verrecchia, F. (2020). The YAP/TEAD Axis as a New Therapeutic Target in Osteosarcoma: Effect of Verteporfin and CA3 on Primary Tumor Growth. *Cancers (Basel)* 12, 3847.
- Mukhopadhyay, G., Doherty, P., Walsh, F.S., Crocker, P.R., and Filbin, M.T. (1994). A novel role for myelin-associated glycoprotein as an inhibitor of axonal regeneration. *Neuron* 13, 757–767.
- Murakoshi, H., Wang, H., and Yasuda, R. (2011). Local, persistent activation of Rho GTPases during plasticity of single dendritic spines. *Nature* 472, 100–104.
- Nagai, J., Owada, K., Kitamura, Y., Goshima, Y., and Ohshima, T. (2016). Inhibition of CRMP2 phosphorylation repairs CNS by regulating neurotrophic and inhibitory responses. *Exp. Neurol.* 277, 283–295.
- Neukirchen, D., and Bradke, F. (2011). Cytoplasmic linker proteins regulate neuronal polarization through microtubule and growth cone dynamics. *J. Neurosci.* 31, 1528–1538.
- Omotade, O.F., Pollitt, S.L., and Zheng, J.Q. (2017). Actin-based growth cone motility and guidance. *Mol. Cell. Neurosci.* 84, 4–10.
- Pertz, O. (2010). Spatio-temporal Rho GTPase signaling - where are we now? *J. Cell Sci.* 123, 1841–1850.
- Quraishy, S., Forbes, L.H., and Andrews, M.R. (2018). The Extracellular Environment of the CNS: Influence on Plasticity, Sprouting, and Axonal Regeneration after Spinal Cord Injury. *Neural Plast.* 2018, 2952386.
- Racchetti, G., D'Alessandro, R., and Meldolesi, J. (2012). Astrocyte stellation, a process dependent on Rac1 is sustained by the regulated exocytosis of en-largeosomes. *Glia* 60, 465–475.
- Renthal, W., Tochitsky, I., Yang, L., Cheng, Y.C., Li, E., Kawaguchi, R., Geschwind, D.H., and Woolf, C.J. (2020). Transcriptional Reprogramming of Distinct Peripheral Sensory Neuron Subtypes after Axonal Injury. *Neuron* 108, 128–144.e9.
- Riedl, J., Crevenna, A.H., Kessenbrock, K., Yu, J.H., Neukirchen, D., Bista, M., Bradke, F., Jenne, D., Holak, T.A., Werb, Z., et al. (2008). Lifefact: a versatile marker to visualize F-actin. *Nat. Methods* 5, 605–607.
- Ruschel, J., and Bradke, F. (2018). Systemic administration of epothilone D improves functional recovery of walking after rat spinal cord contusion injury. *Exp. Neurol.* 306, 243–249.
- Ruschel, J., Hellal, F., Flynn, K.C., Dupraz, S., Elliott, D.A., Tedeschi, A., Bates, M., Sliwinski, C., Brook, G., Dobrindt, K., et al. (2015). Axonal regeneration. Systemic administration of epothilone B promotes axon regeneration after spinal cord injury. *Science* 348, 347–352.
- Sabelström, H., Stenudd, M., Réu, P., Dias, D.O., Elfineh, M., Zdunek, S., Damberg, P., Göritz, C., and Frisén, J. (2013). Resident neural stem cells restrict tissue damage and neuronal loss after spinal cord injury in mice. *Science* 342, 637–640.
- Sami, A., Selzer, M.E., and Li, S. (2020). Advances in the Signaling Pathways Downstream of Glial-Scar Axon Growth Inhibitors. *Front. Cell. Neurosci.* 14, 174.
- Sandner, B., Puttagunta, R., Motsch, M., Bradke, F., Ruschel, J., Blesch, A., and Weidner, N. (2018). Systemic epothilone D improves hindlimb function after spinal cord contusion injury in rats. *Exp. Neurol.* 306, 250–259.
- Santos, T.E., Schaffran, B., Broguière, N., Meyn, L., Zenobi-Wong, M., and Bradke, F. (2020). Axon Growth of CNS Neurons in Three Dimensions Is Amoeboid and Independent of Adhesions. *Cell Rep.* 32, 107907.
- Sarmiere, P.D., and Bamburg, J.R. (2004). Regulation of the neuronal actin cytoskeleton by ADF/cofilin. *J. Neurobiol.* 58, 103–117.
- Schachtrup, C., Ryu, J.K., Helmick, M.J., Vagena, E., Galanakis, D.K., Degen, J.L., Margolis, R.U., and Akassoglou, K. (2010). Fibrinogen triggers astrocyte scar formation by promoting the availability of active TGF- β after vascular damage. *J. Neurosci.* 30, 5843–5854.
- Schelski, M., and Bradke, F. (2017). Neuronal polarization: From spatiotemporal signaling to cytoskeletal dynamics. *Mol. Cell. Neurosci.* 84, 11–28.
- Schwab, M.E., and Strittmatter, S.M. (2014). Nogo limits neural plasticity and recovery from injury. *Curr. Opin. Neurobiol.* 27, 53–60.
- Shevtsova, Z., Malik, J.M., Michel, U., Bähr, M., and Kügler, S. (2005). Promoters and serotypes: targeting of adeno-associated virus vectors for gene transfer in the rat central nervous system in vitro and in vivo. *Exp. Physiol.* 90, 53–59.
- Silver, D.J., and Silver, J. (2014). Contributions of chondroitin sulfate proteoglycans to neurodevelopment, injury, and cancer. *Curr. Opin. Neurobiol.* 27, 171–178.
- Simpson, C.P., Bolch, S.N., Zhu, P., Weidert, F., Dinculescu, A., and Lobanova, E.S. (2019). Systemic Delivery of Genes to Retina Using Adeno-Associated Viruses. *Adv. Exp. Med. Biol.* 1185, 109–112.
- Smith, G.M., and Gallo, G. (2018). The role of mitochondria in axon development and regeneration. *Dev. Neurobiol.* 78, 221–237.
- Socodato, R., Portugal, C.C., Canedo, T., Rodrigues, A., Almeida, T.O., Henriques, J.F., Vaz, S.H., Magalhães, J., Silva, C.M., Baptista, F.I., et al. (2020). Microglia Dysfunction Caused by the Loss of Rhoa Disrupts Neuronal Physiology and Leads to Neurodegeneration. *Cell Rep.* 31, 107796.
- Sofroniew, M.V. (2005). Reactive astrocytes in neural repair and protection. *Neuroscientist* 11, 400–407.
- Sotiropoulos, A., Gineitis, D., Copeland, J., and Treisman, R. (1999). Signal-regulated activation of serum response factor is mediated by changes in actin dynamics. *Cell* 98, 159–169.
- Stepanova, T., Slemmer, J., Hoogenraad, C.C., Lansbergen, G., Dortland, B., De Zeeuw, C.I., Grosveld, F., van Cappellen, G., Akhmanova, A., and Galjart, N. (2003). Visualization of microtubule growth in cultured neurons via the use of EB3-GFP (end-binding protein 3-green fluorescent protein). *J. Neurosci.* 23, 2655–2664.
- Stern, S., Sinske, D., and Knöll, B. (2012). Serum response factor modulates neuron survival during peripheral axon injury. *J. Neuroinflammation* 9, 78.
- Steward, O., Zheng, B., and Tessier-Lavigne, M. (2003). False resurrections: distinguishing regenerated from spared axons in the injured central nervous system. *J. Comp. Neurol.* 459, 1–8.
- Subauste, M.C., Von Herrath, M., Benard, V., Chamberlain, C.E., Chuang, T.-H., Chu, K., Bokoch, G.M., and Hahn, K.M. (2000). Rho family proteins modulate rapid apoptosis induced by cytotoxic T lymphocytes and Fas. *J. Biol. Chem.* 275, 9725–9733.
- Sun, W., Cornwell, A., Li, J., Peng, S., Osorio, M.J., Aalling, N., Wang, S., Benraiss, A., Lou, N., Goldman, S.A., and Nedergaard, M. (2017). SOX9 Is an Astrocyte-Specific Nuclear Marker in the Adult Brain Outside the Neurogenic Regions. *J. Neurosci.* 37, 4493–4507.
- Tedeschi, A., Dupraz, S., Laskowski, C.J., Xue, J., Ulas, T., Beyer, M., Schultze, J.L., and Bradke, F. (2016). The Calcium Channel Subunit

- Alpha2delta2 Suppresses Axon Regeneration in the Adult CNS. *Neuron* 92, 419–434.
- Tedeschi, A., Dupraz, S., Curcio, M., Laskowski, C.J., Schaffran, B., Flynn, K.C., Santos, T.E., Stern, S., Hilton, B.J., Larson, M.J.E., et al. (2019). ADF/Cofilin-Mediated Actin Turnover Promotes Axon Regeneration in the Adult CNS. *Neuron* 103, 1073–1085.e6.
- Tönges, L., Günther, R., Suhr, M., Jansen, J., Balck, A., Saal, K.A., Barski, E., Nentied, T., Götz, A.A., Koch, J.C., et al. (2014). Rho kinase inhibition modulates microglia activation and improves survival in a model of amyotrophic lateral sclerosis. *Glia* 62, 217–232.
- Tuszynski, M.H., and Steward, O. (2012). Concepts and methods for the study of axonal regeneration in the CNS. *Neuron* 74, 777–791.
- Udvadia, A.J., Köster, R.W., and Skene, J.H. (2001). GAP-43 promoter elements in transgenic zebrafish reveal a difference in signals for axon growth during CNS development and regeneration. *Development* 128, 1175–1182.
- Vartiainen, M.K., Guettler, S., Larijani, B., and Treisman, R. (2007). Nuclear actin regulates dynamic subcellular localization and activity of the SRF cofactor MAL. *Science* 316, 1749–1752.
- Wang, X.W., Yang, S.G., Zhang, C., Hu, M.W., Qian, J., Ma, J.J., Zhang, Y., Yang, B.B., Weng, Y.L., Ming, G.L., et al. (2020). Knocking Out Non-muscle Myosin II in Retinal Ganglion Cells Promotes Long-Distance Optic Nerve Regeneration. *Cell Rep.* 31, 107537.
- Woeste, M.A., Stern, S., Raju, D.N., Grahn, E., Dittmann, D., Gutbrod, K., Dörmann, P., Hansen, J.N., Schonauer, S., Marx, C.E., et al. (2019). Species-specific differences in nonlysosomal glucosylceramidase GBA2 function underlie locomotor dysfunction arising from loss-of-function mutations. *J. Biol. Chem.* 294, 3853–3871.
- Ylera, B., Ertürk, A., Hellal, F., Nadrigny, F., Hurtado, A., Tahirovic, S., Oudega, M., Kirchhoff, F., and Bradke, F. (2009). Chronically CNS-injured adult sensory neurons gain regenerative competence upon a lesion of their peripheral axon. *Curr. Biol.* 19, 930–936.
- Yu, P., Santiago, L.Y., Katagiri, Y., and Geller, H.M. (2012). Myosin II activity regulates neurite outgrowth and guidance in response to chondroitin sulfate proteoglycans. *J. Neurochem.* 120, 1117–1128.
- Yu, X., Nagai, J., and Khakh, B.S. (2020). Improved tools to study astrocytes. *Nat. Rev. Neurosci.* 21, 121–138.
- Zhang, Y., Chen, K., Sloan, S.A., Bennett, M.L., Scholze, A.R., O'Keeffe, S., Phatnani, H.P., Guarneri, P., Caneda, C., Ruderisch, N., et al. (2014). An RNA-sequencing transcriptome and splicing database of glia, neurons, and vascular cells of the cerebral cortex. *J. Neurosci.* 34, 11929–11947.
- Zhao, W., Chai, Y., Hou, Y., Wang, D.W., Xing, J.Q., Yang, C., and Fang, Q.M. (2017). Mechanisms responsible for the inhibitory effects of epothilone B on scar formation after spinal cord injury. *Neural Regen. Res.* 12, 478–485.
- Zhu, Y., Romero, M.I., Ghosh, P., Ye, Z., Charnay, P., Rushing, E.J., Marth, J.D., and Parada, L.F. (2001). Ablation of NF1 function in neurons induces abnormal development of cerebral cortex and reactive gliosis in the brain. *Genes Dev.* 15, 859–876.

STAR★METHODS

KEY RESOURCES TABLE

REAGENT or RESOURCE	SOURCE	IDENTIFIER
Antibodies		
mouse anti-tubulin β 3 (Tuj-1)	Biolegend	Cat#801201
rabbit anti-βIII-tubulin	Sigma	Cat#T2200
rabbit anti-MLC 2	Cell Signaling	Cat#3672
rabbit anti-MLC 2	Thermo Scientific	Cat#PA5-17624
mouse anti-phospho-MLC 2 (Ser19)	Cell Signaling	Cat#3675
rabbit anti-phospho-MLC 2 (Ser20)	Abcam	Cat#ab2480
mouse anti-phospho-MLC 2 (Ser19)	Thermo Scientific	Cat#MA5-15163
mouse anti-Cofilin	Abcam	Cat# ab54532
rabbit anti-Cofilin	Cell Signaling	Cat#5175
rabbit anti-phospho-Cofilin (Ser3)	Cell Signaling	Cat#3313
rabbit anti-Glial Fibrillary Acidic Protein (GFAP)	Dako	Cat#Z0334
rabbit anti-Glial Fibrillary Acidic Protein (GFAP)	Sigma	Cat#G3893
chicken anti-Glial Fibrillary Acidic Protein (GFAP)	Millipore	Cat#AB5541
mouse anti-CSPGs	Sigma	Cat#8035
mouse anti-tubulin alpha	Sigma	Cat#T5168
mouse anti-GAPDH	Acris	Cat# ACR001P
rabbit anti-RhoA	Santa Cruz	Cat#sc-179
chicken anti-GFP	Abcam	Cat#ab13970
rabbit anti-SRF	Cell Signaling	Cat#5147
rabbit anti-YAP	Cell Signaling	Cat#14074
mouse anti-YAP	Santa Cruz	Cat#sc-101199
goat anti-SOX9	R&D Systems	Cat#AF3075
rabbit anti-Aldh1I1	Abcam	Cat#ab87117
rabbit anti-5-HT	Immunostar	Cat# 20080
chicken anti-Vimentin	Thermo Scientific	Cat#PA1-16759
goat anti-mouse IgG (H+L), Alexa Fluor 555 conjugated	Invitrogen	Cat#A21422
goat anti-rabbit IgG (H+L), Alexa Fluor 555 conjugated	Invitrogen	Cat#A21429
goat anti-mouse IgG (H+L), Alexa Fluor 488 conjugated	Invitrogen	Cat#A11029
goat anti-rabbit IgG (H+L), Alexa Fluor 488 conjugated	Invitrogen	Cat#A11034
goat anti-rabbit IgG (H+L), Alexa Fluor 594 conjugated	Invitrogen	Cat#A11037
donkey anti-rabbit IgG (H+L) Alexa Fluor 488 conjugated	Thermo Scientific	Cat# A-21206
donkey anti-rabbit IgG (H+L), Alexa Fluor 594 conjugated	Invitrogen	Cat# A21207
donkey anti-goat IgG (H+L) Alexa Fluor 488 conjugated	Thermo Scientific	Cat#A-11055

(Continued on next page)

Continued

REAGENT or RESOURCE	SOURCE	IDENTIFIER
donkey anti-rabbit IgG (H+L) Alexa Fluor 647 conjugated	Thermo Scientific	Cat#A-31573
goat anti-chicken IgG (H+L), Alexa Fluor 488 conjugated	Invitrogen	Cat#A11039
donkey anti-chicken IgY (IgG) (H+L) Alexa Fluor 594 conjugated	Jackson ImmunoResearch	Cat#703-585-155
Donkey Anti-Chicken IgY Alexa Fluor 488 conjugated	Jackson ImmunoResearch	Cat#703-545-155
sheep anti-mouse IgG, ECL Antibody, HRP conjugated	GE Healthcare	Cat#NA931
donkey anti-rabbit IgG, ECL Antibody, HRP conjugated	GE Healthcare	Cat#NA931
Phalloidin, Alexa Fluor 350 conjugated	Thermo Scientific	Cat#A22281
Phalloidin, Alexa Fluor 350 conjugated	Thermo Scientific	Cat#R415
Phalloidin, Atto 647 conjugated	Sigma	Cat#65906
DAPI	Thermo Scientific	Cat#62248
Bacterial and virus strains		
AAV1-eGFP virus	UPenn Vector Core	Cat#AV-1-PV0101
AAV1-RFP virus	UPenn Vector Core	custom made, N/A
AAV1-CofWT-RFP virus	UPenn Vector Core	custom made, N/A
pENN.AAV.hSyn.H1.eGFP-Cre.WPRE.SV40	Duan et al., 2020	Addgene Cat#105540-AAV1
AAV PHP.eB pAAV-CAG-tdTomato (codon diversified)	Simpson et al., 2019	Addgene Cat#59462-PHPeB
Chemicals, peptides, and recombinant proteins		
HBSS	GIBCO	Cat#14025-053
HEPES	GIBCO	Cat#15630-56
Trypsin	Worthington	Cat#LS003703
DNase	Worthington	Cat#LS002007
Neurobasal medium	GIBCO	Cat#12349-015
B-27 supplement	GIBCO	Cat#17504-044
L-glutamine	GIBCO	Cat#25030-024
Penicillin/Streptomycin (PenStrep) antibiotics	GIBCO	Cat#15140122
Horse serum	Pan Biotech	Cat#P30-0712
Poly-L-lysine	Sigma	Cat#P2636
Laminin	Roche	Cat#11243217001
Chicken Extracellular Chondroitin Sulfate Proteoglycans (CSPGs)	Merck Millipore	Cat#CC117
Latrunculin B	Cayman Chemical	Cat#10010631
Cytochalasin D	Enzo	Cat#BML-T109-0001
Jasplakinolide	Cayman Chemical	Cat#Cay11705
Blebbistatin	Sigma	Cat#B0560
Nocodazole	Sigma	Cat#M1404
Taxol	Cayman Chemical	Cat#10461-25
Verteporfin	Sigma	Cat# SML0534
CA3	Sigma	Cat# SML2647
Trypsin/EDTA	GIBCO	Cat#25300-054
Trypsin	Thermo Scientific	Cat#25200-056

(Continued on next page)

Continued

REAGENT or RESOURCE	SOURCE	IDENTIFIER
Collagenase type I	Worthington	Cat#LS004196
10xMEM	GIBCO	Cat#21430-020
50x MEM amino acids	GIBCO	Cat#11130-036
100x MEM nonessential amino acids	GIBCO	Cat#11140-035
Phosphate buffered saline (PBS)	AppliChem	Cat#A0965,9050
Sucrose	Fluka	Cat#84100
Fetal bovine serum	Thermo Scientific	Cat#10500064
Fluoromount	Sigma	Cat#F4680-25
Phosphatase inhibitor	Roche	Cat#04906837001
Protease inhibitor	Roche	Cat#11836170001
Bradford reagent	AppliChem	Cat#A6932
Ponceau S	AppliChem	Cat#A2935
ECL (SuperSignal Dura West)	Thermo Scientific	Cat#34076
FastGreen	Sigma	Cat# 68724
M-1 embedding matrix	Thermo Scientific	Cat#1310
Goat serum	Invitrogen	Cat#16210064
Donkey serum	Jackson ImmunoResearch	Cat#JIM-017-000-121
Silicone fluid	Shin-Etsu	Cat#HIVAC-F-4
Mineral oil	Sigma	Cat#M8410
CUBIC-L	TCI Chemicals	Cat#T3740
CUBIC-R+	TCI Chemicals	Cat#T3741
Critical commercial assays		
Nucleofector Kits for Mouse Neurons	Lonza	Cat#VPG-1001
F- to G-actin ratio assay kit	Cytoskeleton	Cat#BK037
Experimental models: Organisms/strains		
Mouse: <i>nestin-Cre</i>	Jackson Laboratories	Stock No: 003771
Mouse: <i>synapsin I-Cre</i>	Jackson Laboratories	Stock No: 003966
Mouse: <i>GFAP-Cre</i>	Jackson Laboratories	Stock No: 024098
Mouse: <i>RhoA^{f/f}</i>	Jackson et al., 2011	N/A
Mouse: <i>nestin Cre, RhoA^{f/f}</i>	Dupraz et al., 2019	N/A
Mouse: <i>synapsin I Cre, RhoA^{f/f}</i>	This publication	N/A
Mouse: <i>GFAP Cre, RhoA^{f/f}</i>	This publication	N/A
Recombinant DNA		
pCMV-LifeAct-EGFP (GFP-Lifeact)	Riedl et al., 2008	N/A
pCMV-EB3-mCherry (EB3-mCherry)	Stepanova et al., 2003	N/A
pEGFP-C1 (eGFP)	Clontech	GenBank Accession #U55761
pcDNA3-EGFP-RhoA-wt (RhoAwt-eGFP)	Subauste et al., 2000	Addgene Cat#12965
pEGFP-C3.1-MRLC1 (MLCca-eGFP)	Beach et al., 2011	Addgene Cat#36580
SRFcontrol (SRFco)/SRF constitutive active (SRFc)	Stern et al., 2012	N/A
Software and algorithms		
ImageJ	NIH, USA	N/A
Photoshop	Adobe, USA	N/A
Canvas X3	ACD Systems, USA	N/A
BioRender	BioRender, Canada	N/A
AxioVision	Zeiss	N/A
ZEN	Zeiss	N/A
SoftWoRx 3.5.0	Applied Precision	N/A

(Continued on next page)

Continued

REAGENT or RESOURCE	SOURCE	IDENTIFIER
MetaMorph Microscopy Automation and Image Analysis Software	Molecular Devices	N/A
Imaris 9.1	Bitplane	N/A
Other		
35 mm glass bottom dish, No. 1.5 Coverslip, 20 mm, Uncoated	MatTek	Cat#P35G-1.5-20-C
6-well plates	Thermo Scientific	Cat#140675
4-well plates	Thermo Scientific	Cat#179820
13 mm coverslip	Marienfeld	Cat#01-11530
Immobilon-PSQ PVDF Membrane	Millipore	Cat#ISEQ00010
X-ray film	Thermo Scientific	Cat#34076
ImmEdge pen	Vector laboratories	Cat#H-4000
Microknife	FST	Cat#10316-14
Forceps	FST	Cat#11252-00
Amaxa Nucleofector device	Lonza	Nucleofector II, N/A
Fluorescence microscope	Zeiss	Axio Observer D1, N/A
Live cell microscope	Applied Precision	DeltaVision RT, N/A
Confocal microscope	Zeiss	LSM700, N/A
Confocal microscope	Zeiss	LSM800, N/A
2-photon microscope	Zeiss	LSM 7MP, N/A
Plan-Apochromat 100x NA 1.4 objective	Zeiss	N/A
Plan-Apochromat 60x/1.42 infinity/0.17/ FN26.5 objective	Olympus	N/A
Plan-Apochromat 63x/1.40 Oil DIC M27	Zeiss	N/A
EC Plan-Neofluar 10x/0.30 M27 objective	Zeiss	N/A
16 × , 0.80 NA objective	Nikon	Cat#N16XLWD-PF
Photometrics CoolSnap HQ camera	Roper Scientific	N/A
CCD camera	Zeiss	N/A
Heating System	Ibidi	Cat#10918
Heating Insert μ-Dish 35 mm high for ibidi Heating System	Ibidi	Cat#10934
Gas Incubation System for CO ₂	Life Imaging Services	N/A
Cryostat	Leica	Cat#CM3050S
CaWomat	Cawo	Cat#2000IR
Pneumatic picopump (picospritzer)	WPI	Cat#SYS-PV820

RESOURCE AVAILABILITY**Lead contact**

Further information and requests for resources and reagents should be directed to and will be fulfilled by the lead contact, Frank Bradke (Frank.Bradke@dzne.de).

Materials availability

This study did not generate new unique reagents.

Data and code availability

All data reported in this paper will be shared by the lead contact upon request.

This paper does not report original code. Permutation tests were performed using a custom script “permutation_test 0.18” implemented in Python (2.7.3 version) including Pandas and NumPy libraries. The script is available for download in the Python Package Index (https://pypi.org/pypi/permutation_test). Graphical abstract, Figure 1A, 2A, 3A, 4 A, 4E, 6A, and 8A were created with BioRender (<https://biorender.com>).

Any additional information required to reanalyze the data reported in this paper is available from the lead contact upon request.

EXPERIMENTAL MODEL AND SUBJECT DETAILS

Animals

All animal experiments were performed in accordance with the Animal Welfare Act and the guidelines of the Landesamt für Natur, Umwelt und Verbraucherschutz (LANUV). Mouse lines with Cre recombinase expression under the control of the nestin (nestin-Cre, Stock No: 003771), synapsin I (synapsin-Cre, Stock No: 003966) or GFAP (GFAP-Cre, Stock No: 024098) promotor were purchased from Jackson Laboratories. *Rhoa^{fl/fl}* mice have been previously described (Jackson et al., 2011). Generation of *nestin-Cre, rhoA^{fl/fl}, synapsin-Cre, rhoA^{fl/fl}* and GFAP-Cre, *rhoA^{fl/fl}* was achieved by crossing the *rhoA^{fl/fl}* line with the appropriate Cre recombinase line and confirmed with PCR genotyping (Dupraz et al., 2019). For primary cell culture of cerebellar neurons or astrocytes, mice of both sexes of the indicated age were used. *Nestin/synapsin/GFAP-Cre^{tg/-}, rhoA^{fl/fl}* were compared to *nestin/synapsin/GFAP-Cre^{-/-}, rhoA^{fl/fl}* control mice. For *in vivo* experiments, mice of both sexes between 3 and 6 months of age were used. *Nestin/synapsin/GFAP-Cre^{tg/-}, rhoA^{fl/fl}* were compared to *nestin/synapsin/GFAP-Cre^{-/-}, rhoA^{fl/fl}* or *rhoA^{fl/fl}* control mice as indicated.

METHOD DETAILS

Primary cell culture

Cerebellar neurons

Cerebellar neurons were prepared as described previously (Woeste et al., 2019). In brief, cerebella of postnatal day 2 or 6–10 mice were dissected and placed in sterile HBSS (GIBCO, Cat#14025-053)/7 mM HEPES (GIBCO, Cat#15630-56). Meninges were removed and the tissue was digested in trypsin (Worthington, Cat#LS003703)/DNase (Worthington, Cat#LS002007) solution. The tissue was washed three times in HBSS/7 mM HEPES/ 5 µg/ml DNase. Cells were dissociated with glass Pasteur pipettes, centrifuged at 800 × g at 4°C for 5 min, and washed twice with HBSS/7 mM HEPES. Finally, the cells were resuspended in complete Neurobasal medium (95% Neurobasal medium (GIBCO, Cat#12349-015)), 2% B-27 supplement (GIBCO, Cat#17504-044), 2 mM L-glutamine (GIBCO, Cat#25030-024), 1% PenStrep antibiotics (GIBCO, Cat#15140122), 2% horse serum (Pan Biotech, Cat#P30-0712) counted and plated in a density of 200–400 cells/mm². As indicated, neurons were transfected with the expression plasmids GFP-Lifeact (Riedl et al., 2008), EB3-mCherry (a gift from Ana Akmanova; Stepanova et al., 2003), eGFP (Clontech), RhoAwt-eGFP (a gift from Gary Bokoch; Addgene plasmid # 12965; Subauste et al., 2000) and MLCca-eGFP (a gift from Tom Egelhoff; Addgene plasmids # 35681; Beach et al., 2011) (8 µg each) following the Amaxa Nucleofector II device instructions (Lonza). Cofilin overexpression was done by viral transduction with either AAV-RFP control or AAV-CofWT-RFP virus (1–5×10¹³ genome copies/ml, custom made, UPenn Vector Core). For live cell imaging, neurons were grown on 35 mm glass-bottom dishes (MatTek, Cat#P35G-1.5-20-C). For protein analysis on 6-well plates (Thermo Scientific, Cat#140675) and for immunocytochemistry, cells were cultured on 13 mm glass coverslips (Marienfeld, Cat#01-11530) contained in 4-well dishes (Thermo Scientific, Cat#179820). All growth surfaces were first coated with 1 mg/ml poly-L-lysine (PLL, Sigma, Cat#P2636-1G). For CSPG stimulation, this was followed by 5 mg/ml laminin (Roche, Cat#11243217001) for control or 3.5 µg/ml CSPGs (Merck Millipore, Cat#CC117) in 5 mg/ml laminin for inhibitory treatment. In fluorescent live cell experiments or F- to G-actin ratio assay 5 µg/ml CSPGs were added directly to the media. For myelin stimulation, either 30 mM HEPES for control or 5 µg myelin in 30 mM HEPES for inhibitory treatment was vacuum-dried on the growth surface. After 4 h in culture, the drugs latrunculin B (1 µM, Cayman Chemical, Cat#10010631), cytochalasin D (1 µM, Enzo, Cat#BML-T109-0001), blebbistatin (5 µM, Sigma, Cat#B0560), nocodazole (75 nM, Sigma, Cat#M1404) and taxol (10 nM, Cayman Chemical, Cat#10461-25) were added to the media as indicated. Cells were grown for 36 h in total at 36.5°C in a humidified atmosphere containing 5% CO₂.

Dorsal root ganglion (DRG) neurons

DRG neurons from adult mice were dissected, dissociated, and cultured as previously described (Tedeschi et al., 2019). In brief, L4–5 DRGs were dissected on ice and collected in ice-cold HBSS/7 mM HEPES. The surrounding connective tissue was removed and the ganglia were cut open and incubated in collagenase type I (3000 U/ml, Worthington, Cat#LS004196) for 45 min at 37°C, washed once with HBSS, followed by 15 min incubation in trypsin (0.25%, Thermo Fisher, Cat#25200-056) at 36.5°C. Enzymatic digestion was stopped by addition of complete Neurobasal medium containing 5% horse serum. Neurons were recovered by centrifugation at 630 rpm for 5 min and resuspended in complete Neurobasal medium. Dissociated neurons were cultured on 13 mm glass coverslips contained in 4-well dishes and coated with poly-L-lysine (1 mg/ml) followed by 5 mg/ml laminin for control or 3.5 µg/ml CSPGs in 5 mg/ml laminin for inhibitory treatment and incubated at 36.5°C in a humidified atmosphere containing 5% CO₂ for 48 h.

Astrocytes

Cortices of postnatal day 2–5 mice were dissected and placed in sterile HBSS/7 mM HEPES. Meninges were removed and the tissue was digested at 37°C in 0.05% trypsin/EDTA (GIBCO, Cat#25300-054)/7 mM HEPES solution for 10 min, followed by three washes with HBSS/7 mM HEPES/ 5 µg/ml DNase. Cells were dissociated by pipetting through glass pasteur pipettes, centrifuged at 800 × g at 4°C for 5 min, and resuspended in HBSS/7 mM HEPES. Finally, cells were plated in a density of 400–800 cells/mm² in MEM-HS (10% 10xMEM (GIBCO, Cat#21430-020), 0.3% NaHCO₃, 6.7% Glucose, 2 mM L-glutamine (GIBCO, Cat#25030-024), 2% 50x MEM amino acids (GIBCO, Cat#11130-036), 2% 100x MEM nonessential amino acids (GIBCO, Cat#11140-035), 10% horse serum).

Where indicated, neurons were transfected with the expression plasmids eGFP or RhoAwt-eGFP (8 µg each) or, for SRF overexpression, with a mixture of SRFcontrol/eGFP or SRFca/eGFP plasmid (8/2 µg each) following the Amaxa Nucleofector II device instructions. SRF plasmids were a gift from Bernd Knöll (Stern et al., 2012). For protein analysis cells were grown on 6-well plates and for immunocytochemistry and the scratch assay on 13 mm glass coverslips contained in 4-well dishes. All growth surfaces were coated with 10 µg/ml PLL. After 1 h in culture, media was changed to fresh MEM-HS and after 4 h in culture, the drugs latrunculin B, cytochalasin D, jasplakinolide (5 nM, Cayman Chemical, Cat#Cay11705), blebbistatin, taxol (100 nM), verteprofin (0.5 µM, Sigma, Cat#SML0534) and CA3 (0.75 µM, Sigma, Cat# SML2647) were added to the media as indicated. Cells were grown for 48 h in total.

Immunocytochemistry

All solutions were prepared in PBS (AppliChem, Cat#A0965,9050). At indicated time points, primary cells were fixed with 4% paraformaldehyde (Merck Millipore, Cat#104005)/ 4% sucrose (Fluka, Cat#84100) for 15 min. Subsequently, free aldehyde groups were quenched with 0.1 M glycine and cells were washed 3 times with PBS. After permeabilization with 0.1% Triton X-100 for 2 min, cells were washed another 3 times with PBS. Cells were then incubated with blocking solution (2% fetal bovine serum (Thermo Scientific, Cat#10500064), 2% bovine serum albumin, 0.2% fish gelatin) for 30 min. Primary antibodies (Tuj-1 1:1000, Biolegend, Cat#801201; MLC 1:100, Cell Signaling, Cat#3672; pMLC 1:200, Cell Signaling, Cat#3675; Cof 1:100, Abcam, Cat#ab54532; pCof 1:100, Cell Signaling, Cat#3313; GFAP 1:500, Dako, Cat#Z0334; GFAP 1:500, Sigma, Cat#G3893; CSPGs 1:500, Sigma, Cat#C8035; alpha-tubulin 1:2000, Sigma, Cat#T5168; SRF 1:200, Cell Signaling, #Cat5147; YAP 1:500, Santa Cruz, Cat#sc-101199; YAP 1:200, Cell Signaling, Cat#14074 as well as bIII-tubulin 1:1000, Sigma, Cat#T2200 for high-resolution imaging) were added in 10% blocking solution for 1 h. After 4 rinses in PBS, cells were incubated with Phalloidin labeled with Rhodamine, Alexa Fluor 350 or Atto 647 for high-resolution imaging (1:50 or 1:200, Thermo Scientific, Cat#A22281, Cat#R415 or Sigma Cat#65906) and the appropriate Alexa Fluor secondary antibodies (anti-mouse 555 or 488; anti-rabbit 555, 594 or 488, 1:500, Invitrogen) for 30 min. When necessary, cells were counterstained with 4',6-diamidino-2-phenylindole (DAPI, 0.5 µg/ml, Thermo Scientific, Cat#62248) for 5 min. Finally, cells were washed another 3 times in PBS before mounting with Fluoromount (Sigma, Cat#F4680-25) onto microscope slides. Images were randomly taken with an Axio Observer D1 microscope (Zeiss) and analyzed using ImageJ analysis software (NIH, USA). Neurite outgrowth was calculated by imaging and measuring the longest neurite of each neuron. To quantify the amount of F-actin, pMLC/MLC, pCof/Cof, GFAP, CSPGs and alpha-tubulin, the mean gray value in an area of interest was measured and the background subtracted to obtain the fluorescence intensity. High-resolution imaging was done by Airyscan super-resolution confocal microscopy using an LSM800 confocal microscope (Zeiss) and analyzed using ImageJ analysis software. Astrocyte morphology was assessed from the ratio of cell diameter at the widest and narrowest part, whereby an evenly round cell has a ratio of 1. The number of independent experiments for each condition is indicated in the corresponding figure legend.

Live cell microscopy

In order to observe primary cells under optimal growth conditions with 36.5°C and 5% CO₂, a heating system (ibidi) together with a CO₂ regulated chamber and an active gas mixer (Solent Scientific, Live Imaging Science) was connected to the live cell microscope setups.

Growth cone dynamics

To determine growth cone dynamics, phase contrast live cell microscopy was performed as described previously using the same setup (Tedeschi et al., 2019). Briefly, an Axio Observer D1 microscope (Zeiss) with a Plan-Apochromat 100x NA 1.4 objective (Zeiss) connected to a CCD camera (AxioCam Zeiss) was used for imaging. Pictures were recorded and analyzed using AxioVision or ZEN microscope (Zeiss) and ImageJ analysis software. Dynamics of individual growth cones were quantified over a time period of 3 min by measuring changes of growth cone area every 10 s. To this end, growth cones were outlined manually using MetaMorph Microscopy Automation and Image Analysis Software (Molecular Devices). Growth cone outlines were pasted onto the following images and changes of growth cone area between single images were added together to calculate the total growth cone area change over time. The number of independent experiments for each condition is indicated in the corresponding figure legend.

Microtubule dynamics

Fluorescent live cell microscopy to assess microtubule dynamics was performed using the same DeltaVision RT setup (Applied Precision) described in Dupraz et al. (2019). Simultaneous mCherry/GFP images of the growth cone area were acquired every 3 s for 3 min using a PlanApo 60x/1.42 infinity/0.17/FN26.5 objective (Olympus) connected to a Photometrics CoolSnap HQ camera (Roper Scientific) controlled by the imaging software SoftWoRx 3.5.0 (Applied Precision). The analysis of microtubule protrusion was done as described previously (Neukirchen and Bradke, 2011) by measuring the distance of microtubule end tips to the leading edge of the growth cone. Therefore, EB3 fluorescence intensity was measured from the outer boundary of the growth cone to 20 µm along the growth cone using ImageJ analysis software. The number of independent experiments for each condition is indicated in the corresponding figure legend.

Scratch assay

Astrocytes were cultured at high density and grown on 13 mm coverslips until they reached confluence. With a 200 µl pipette tip, a scratch was drawn over the whole coverslip, leaving a ~500 µm wide gap. Cells were fixed at 6, 24, 48 and 72 h and representative images were taken with the Axio Observer DI fluorescence microscope and the gap size was measured based on F-actin immunoreactivity using ImageJ software.

Co-culture of astrocytes and CGNs

For co-culture of astrocytes and cerebellar granule cells (CGNs) both cell types were prepared as described above. The astrocytes were plated in high density on PLL coated 6 well plates. The CGNs were plated at low density on PLL coated glass coverslips with 1 mm thick wax dots on the wax dot side. After the CGNs were attached to the coverslip, the coverslip was flipped onto the astrocytes with the wax dots and the CGNs facing down. With this the CGNs grew close to the astrocytes, sharing the same medium containing secreted molecules but without direct contact. After 36 h immunocytochemistry, microscopy and neurite outgrowth analysis was performed as described above.

Immunoblotting

Primary cells were kept on ice and washed once with PBS, then scraped off the culture dish with ice cold protein lysis buffer (50 mM Tris pH7.4, 150 mM NaCl, 1 mM EDTA, 1% Triton X-100) containing phosphatase (Roche, Cat#04906837001) and protease inhibitors (Roche, Cat#11836170001) and finally incubated for 30 min. Spinal cord tissue was snap frozen in liquid nitrogen immediately after dissection and stored at -80°C until being dissociated with 26 gauge capillary in ice cold lysis buffer. Primary cells as well as tissue lysates were centrifuged for 5 min at 14.000 rpm and the supernatant was collected. Protein concentration in the lysate was determined using Bradford Reagent (Applichem, Cat#A6932) following manufacturer's instructions. Lysates were mixed 6:1 with Laemmli buffer (300 mM Tris pH6.8, 600 mM beta-Mercaptoethanol, 0.1% Bromophenol blue, 60% Glycerol, 6% SDS), boiled at 97°C, fractioned by 10%-12% SDS-polyacrylamide gel electrophoresis (PAGE) and transferred to a polyvinylidene difluoride (PVDF) membrane (Millipore, Cat#ISEQ00010). Ponceau S (Applichem, A2935) staining was used to confirm a uniform transfer of the protein samples. After blocking with 5% nonfat dry milk or 5% BSA in TBS-T (20 mM Tris pH7.6, 137 mM NaCl, 0.1% Tween-20) for 30 min, the membrane was incubated with the indicated primary antibodies (GAPDH 1:20000, Acris, Cat#ACR001P; MLC 1:1000, Cell Signaling, Cat#3672; pMLC 1:1000, Abcam, Cat#ab2480, 3675; Cof 1:1000, Cell Signaling, Cat#5175; pCof 1:1000, Cell Signaling, Cat#3313; GFAP 1:500, Dako, Cat#Z0334; CSPGs 1:500, Sigma, Cat#C8035 and RhoA 1:500, Santa-Cruz, Cat#sc-179) at 4°C overnight. The membrane was rinsed 3 times for 15 min each in TBS-T and incubated with the appropriate horseradish peroxidase conjugated secondary antibodies (1:5000, GE Healthcare, Cat#NA931 or Cat#NA934) for 1 h. For protein detection, the membrane was incubated with enhanced chemiluminescence solution (ECL, SuperSignal West Dura, Thermo Scientific, Cat#34076) and the signal was fixed on X-ray film (Thermo Scientific, Cat#34090) and developed with an automatic CaWomat (Cawo, 2000IR) developer. Protein amount was assessed by quantification of the average mean intensity of the protein bands in ImageJ, subtracted by the background and divided by the protein amount of the corresponding loading control. To record differences in phosphorylation level, first the amount of phospho- and total protein was quantified and then the ratio was done. For F- to G-actin ratio assay the protein amount of F-actin was divided by the protein amount of G-actin for each of the according conditions. Quantification was done on non-saturated immunoblots, but for better visualization immunoblots of higher exposure were shown. Glyceraldehyde-3-phosphate dehydrogenase (GAPDH) was used as protein loading control. The number of independent experiments for each condition is indicated in the corresponding figure legend.

F- to G-actin ratio assay

Filamentous and globular monomeric actin were fractionated from WT and RhoANesKO CGNs using a centrifugation-based F- to G-actin ratio assay kit (Cytoskeleton, BK037). Cultured neurons were lysed and processed according to the manufacturer's guidelines. The resulting fractions were analyzed by immunoblot using an anti-pan actin antibody provided by the kit.

Brain injury

Mice were anaesthetised with an intraperitoneal (i.p) injection of ketamine (100mg/kg body weight) and xylazine (10 mg/kg body weight). Analgesics, antibiotics and eye ointment were administered prior to the surgery and postsurgical care was done according to the authorized animal protocols. The surgical site was prepped and a 5 mm incision made lateral to the cranial midline and posterior to bregma. The fascia overlaying the cranial bone was removed using a scalpel and air-dried. The barrel cortex was identified according to stereotactic coordinates (3.3 mm posterior to bregma, 4.5 mm lateral from midline) and a dental drill used to create a small opening in the cranium. A 27-gauge needle was inserted to a depth of 2.5 mm and held in place for 3 s before removal. The opening was sealed with dental acrylic and the incision sutured. After 3 days mice were sacrificed and the tissue of the lesion site was collected and processed for immunoblotting as described above.

Fiber tracing

Surgeries were completed similarly to as previously described in detail ([Hilton et al., 2019](#)). For all surgical procedures, mice were anaesthetized with isoflurane and kept in deep, reflex-free anesthesia. Analgesics, antibiotics and eye ointment were administered prior to the surgery and postsurgical care was done according to the authorized animal protocols.

Dorsal column sensory axons were traced by injecting AAV encoding GFP into the sciatic nerve. To this end, approximately 2 µl of 1-5x10¹³ genome copies/ml AAV1.CMV.PI.eGFP.WPRE.bGH (AAV-eGFP, UPenn Vector Core facility, Cat#AV-1-PV0101) either alone or in a 1:1 ratio with pENN-AAV.hSyn.H1.eGFP-Cre.WPRE.SV40 (AAV-Cre, Addgene, Cat#105540-AAV1) mixed with 10% Fast-Green (Sigma, Cat# 68724) was injected into the sciatic nerve using a pulled glass capillary connected to a pneumatic picopump (WPI, Cat#SYS-PV820).

Corticospinal axons were traced by injecting AAV encoding TdTomato into the motor cortex. To this end, AAV PHP.eB-CAG-tdTomato alone or mixed in a 1:1 ratio with AAV-Cre (1×10^{13} genome copies/ml) and 10% FastGreen were loaded into a 5 μl Hamilton syringe tipped with a 1 mm removal needle compression fitting (Hamilton, Cat#55750-01) and connected to a UMP3 UltraMicroPump (World Precision Instruments). A burr hole was drilled into the skull at the coordinates 1.5 mm lateral (to the right) of bregma, 0.5 mm caudal, and the needle was lowered at these coordinates to a depth of 0.7 mm ventral to the surface of the brain. 0.5 μl of viral solution was injected at a rate of 0.1 $\mu\text{L}/\text{min}$ and the needle was left in place for 5 min prior to removal from the brain.

Spinal Cord Injury (SCI)

Laceration and crush SCIs

Depending on the experimental paradigm used, a T6-T8 or T10-T12 laminectomy was performed. We transitioned from the more rostral T6-T8 injury model to a T10-T12 injury model to facilitate the imaging of the axons in the unsectioned spinal cord with 2-photon microscopy, given that the sciatic nerve axons travel more dorsally at T12 compared to T8. Furthermore, we transitioned from a laceration injury model to a crush injury model as the latter improves the visualization of whole axon trajectories in the uncleared spinal cord by limiting cell debris. For the analysis of sensory axon regeneration in RhoANesKO mice in [Figure 4](#), the dorsal half (1 mm deep) of the left side of the spinal cord was cut at T8 using a microknife (FST, Cat#10316-14). For subsequent analyses of sensory axon regeneration in [Figures 6](#) and [8](#), a dorsal column lesion was performed by crushing the dorsal columns at T12 to a depth of 0.7 mm with forceps (FST, Cat#11252-00). For analysis of corticospinal axon regeneration in [Figure 8](#), a T12 dorsolateral hemisection was performed using 4 mm Vannas Spring Scissors (FST, Cat#15018-10). To this end, a 26 gauge needle was used to puncture holes in the dura overlying the dorsal horns and the scissor tips were inserted into the holes to cut the dorsal column to a depth of 1 mm. Then, a second cut was made of the left dorsolateral funiculus, with one tip of the scissors in the left hole and the other lateral to the spinal cord to a depth of 1 mm. The lesion was then verified using a 26 gauge needle tip. The muscle layer was sutured with 5-0 suture material (B. Beraun Surgical, Cat#1/8491) and the skin closed with 7-mm skin-closing clips (CellPoint Scientific, Cat#203-1000).

Spinal cord contusion

A dorsal laminectomy at vertebral level T10 was performed. Mice received a midline 65 kdyn spinal cord contusion injury using an Infinite Horizon Impactor and a 1.3 mm impact tip (Precision Systems Instrumentation). Overlying musculature was sutured and skin closed as above. Bladders were manually expressed twice daily until the end of the study period. The order of surgery was randomized across experimental groups and the surgeon was blind to experimental group.

Functional assessment

The Basso Mouse Scale (BMS) was used to assess open field hindlimb function during locomotion following spinal cord contusion as above ([Basso et al., 2006](#)). Mice were tested in the morning, approximately 2 h following bladder expression. Over a period of 4 minutes, two investigators blinded to experimental group scored locomotion using the 10 point (0-9) BMS. Testing was performed on days 1, 3, 5 and 7 after injury, and weekly thereafter for a total of 8 weeks. All BMS data are presented as mean + SEM and were analyzed using a Mixed Effects Model (restricted maximum likelihood) followed by multiple comparisons with Fisher's LSD (GraphPad Prism 9). One WT animal was removed at day 5, two RhoASynKO mice and one RhoAGFAP mouse were removed due to ethical end-point at 7-14 days post-injury. Their data are included in behavior analysis.

Tissue Processing Sectioned Tissue Analyses

Animals were transcardially perfused with 4% paraformaldehyde in 0.1 M PBS and the spinal cord was dissected. Tissue was post-fixed in 4% paraformaldehyde in 0.1 M PBS overnight and then transferred to 30% sucrose in PBS for 3 d. Tissue was embedded in M-1 embedding matrix (Thermo Scientific, Cat#1310), frozen and, with a cryostat (Leica, CM3050S), sliced in 20 or 25 μm thick sagittal sections of the lesion site and transverse sections of the rostral and caudal part. The sections were mounted on microscope slides, framed with hydrophobic ImmEdge pen (Vector laboratories, Cat#H-4000) and dried for 1 h at 37°C. For the axon regeneration analysis in tissue sections in RhoANesKO mice, following 4 washes with TBS-T (50 mM Tris-Cl, pH 8, 150 mM NaCl, 0.2% Triton X-100) and blocking with 5% goat serum (Invitrogen, Cat#16210064) in TBS-T for 1 h, sections were incubated with primary antibodies (GFAP, 1:500, Dako, Cat#Z0334; CSPGs, 1:500, Sigma, Cat#C8035) in blocking solution at 4°C overnight. Sections were rinsed 4 times with TBS-T and incubated with the appropriate Alexa Fluor secondary antibodies (anti-mouse 555 or 488; anti-rabbit 555 or 488, 1:500 Invitrogen) for 1 h, counterstained with DAPI for 5 min and rinsed another 4 times with TBS-T. For analysis of Sox9+ cell density in RhoANesKO mice, sections were rinsed in PBS and blocked with 10% donkey serum (Jackson ImmunoResearch, Cat#017-000-121) in PBS containing 0.1% Triton X-100 (PBST) for 1 h, then incubated overnight with primary antibodies (GFAP, 1:500, Millipore, Cat#AB5541; SOX9, 1:200, Novus, Cat#AF3075; Aldh1l1, 1:250, Abcam, Cat#ab87117) in PBST at room temperature. Sections were then rinsed 3 times with PBS and incubated with the appropriate Alexa Fluor secondary antibodies (anti-goat 488, anti-rabbit 405, anti-chicken 594, Invitrogen) for 2 h, then rinsed 3 times with PBS. For 5-HT and GFAP/Vimentin analysis of tissue in the spinal cord contusion study, following blocking in 10% donkey serum in PBST for 1 h, sections were incubated overnight with a primary antibody to 5-HT (1:15 000, ImmunoStar) in PBST at room temperature, washed 3 times with PBS and incubated in Alexa Fluor secondary antibody anti-rabbit 488 (1:1000) for 2 h. For analysis of the spinal cord contusion injury site, sections were blocked and immunostained as above using primary antibodies to GFAP (Dako, 1:2000) and Vimentin (Thermo, PA1-16759) and appropriate

Alexa Fluor secondary antibodies (anti-rabbit 488, anti-chicken 647). After letting them dry completely, the sections were finally preserved in Fluoromount, covered by coverslips, and stored at 4°C until microscopy.

Tissue Processing Whole Mount Spinal Cords

Sensory axon regeneration

The unsectioned spinal cords were washed 5 times with PTwH (PBS with 0.2% Tween-20, 10 µg/ml heparin) overnight. Permeabilization (80% PTx.2 (1x PBS with 0.2% Tween-20), 20% DMSO, 300 mM glycine) and blocking (84% PTx.2, 10% DMSO, 6% donkey serum (Jackson ImmunoResearch, Cat#JIM-017-000-121) were done at 37°C and 100 rpm shaking overnight. Primary antibodies (GFAP, 1:300, Dako, Cat#Z0334; GFP, 1:500, Abcam, Cat#ab13970) were added in blocking solution at 37°C and 100 rpm shaking for 3 days. The samples were then rinsed 5x with PTwH overnight followed by incubation with secondary Alexa Fluor antibodies (donkey anti-rabbit 594, donkey anti-chicken 488, 1:400, Invitrogen) in blocking solution at 37°C and 100 rpm shaking for 2 days. After, samples were washed 5 times with PTwH overnight and stored at 4°C until imaging.

Corticospinal regeneration

The unsectioned spinal cords were washed 5 times with PBS and then stored in 50% CUBIC-L (TSI Chemicals, Cat#T3740) diluted in dH₂O at room temperature overnight. The following day, samples were then incubated in undiluted CUBIC-L at 37°C with 100 RPM shaking for 3 days. Samples were then washed 5x with PTwH at room temperature overnight. Samples were then blocked with 84% PTx.2, 10% DMSO, 6% donkey serum (Jackson ImmunoResearch, Cat#JIM-017-000-121) at 37°C and 100 rpm shaking overnight. Primary antibody (GFAP, 1:300, Dako, Cat#Z0334) was then added in blocking solution at 37°C and 100 rpm shaking for 3 days. The samples were then rinsed 5x with PTwH overnight followed by incubation with secondary Alexa Fluor antibody (donkey anti-rabbit 488, 1:400, Invitrogen) at 37°C and 100 rpm shaking for 2 days. Samples were then rinsed 5x with PTwH overnight, followed by incubation with 50% CUBIC-R+ (TSI Chemicals, Cat#T3741) diluted in dH₂O at room temperature overnight. Samples were then incubated in undiluted CUBIC-R+ at room temperature and 100 rpm shaking for 2 days. Samples were incubated in Mounting Solution for CUBIC-R+ (TCI Chemicals, Cat#M3294) 1-2 h prior to imaging.

Microscopy and Image Analysis

Tissue section analyses

Images of tissue sections were taken with a LSM700 or LSM780 confocal microscope (Zeiss) equipped with an EC Plan-Neofluar 10x/0.30 M27 objective or a 20X EC Plan-Neufluar objective and a CCD camera (Zeiss). Zen software (Zeiss) was used to calculate average fiber density in sagittal sections. To this end, the lesion epicenter was identified by GFAP staining, and then the number of traced axons at indicated distances from the epicenter was normalized to the number of traced axons 1000 µm caudal to the lesion. While caudal transverse sections were used to confirm comparable tracing efficiency among animals, rostral transverse sections were used to rule out fiber sparing due to incomplete lesion. To analyze SOX9+ cells, two sections corresponding to the lesion epicenter and spaced 100 µm from each other were analyzed for each animal. The Z stack was imported into Imaris and the 3D rendered image was cropped to a 1000 µm x 1000 µm region of interest surrounding the lesion epicenter as defined by absence of GFAP immunoreactivity. The number of Sox9+ dots was counted automatically using Imaris' spot function and averaged for each mouse. For Serotonin (5-HT) analysis, a region of interest corresponding to the ventral horns of each spinal cord image was selected. The region was assigned a pixel value representative of positive immunostaining, whereby pixels above this threshold were summed and averaged for each animal in each experimental group. Threshold and region of interest area were maintained across analysis. For contusion epicenter analysis, serial sagittal sections 200 µm apart throughout the width of the spinal cord were imaged using a LSM780 (Zeiss) confocal microscope. Using ImageJ, GFAP-negative lesion areas were manually traced to calculate lesion area. For each animal, a total lesion volume was calculated, and these averaged for each experimental group.

Whole mount analyses

Whole mount spinal cord imaging and analysis were done as described previously in detail (Hilton et al., 2019). Briefly, images were acquired with a multiphoton setup (LSM 7MP, Zeiss) equipped with a 16x 0.80 NA objective (Nikon, N16XLWD-PF) and a CCD camera (Zeiss). Image processing was done with Imaris software. For sensory axon regeneration analyses, tile scan z stack images were imported into Imaris, the lesion site was identified based on absence of GFAP immunoreactivity and the number of axons in 200 µm bins were manually annotated and normalized to the number found in the bin corresponding to 400 – 200 µm caudal to the lesion site to account for differences in tracing efficacy. For corticospinal axon regeneration analysis, tile scan z stack images were imported into Imaris, the lesion epicenter was identified based on absence of GFAP immunoreactivity and the 3D rendered structure cropped to 2000 µm rostral and 800 µm caudal to the injury. Imaris' Surface function was then used to calculate the total volume of cortico-spinal axons in each area of the spinal cord and normalized to the volume found 2000 – 1800 µm rostral to the lesion site to account for differences in tracing efficacy.

QUANTIFICATION AND STATISTICAL ANALYSIS

Statistical analysis was performed using one-way ANOVA analysis of variance, followed by Bonferroni post test, or using unpaired Student's t test, as indicated in the figure legends. Statistical analysis of axon regeneration *in vivo* was performed by permutation test, as previously described (Tedeschi et al., 2016).